

Submesoscale Currents in the Subtropical Upper Ocean Observed by Long-Term High-Resolution Mooring Arrays

ZHIWEI ZHANG,^{a,b,c} XINCENG ZHANG,^a BO QIU,^d WEI ZHAO,^{a,b,c} CHUN ZHOU,^{a,b,c}
XIAODONG HUANG,^{a,b,c} AND JIWEI TIAN^{a,b,c}

^a *Physical Oceanography Laboratory/IAOS and Frontiers Science Center for Deep Ocean Multispheres and Earth System, Ocean University of China, Qingdao, China*

^b *Pilot National Laboratory for Marine Science and Technology, Qingdao, China*

^c *Sanya Oceanographic Institution, Ocean University of China, Sanya, China*

^d *Department of Oceanography, University of Hawai'i at Mānoa, Honolulu, Hawaii*

(Manuscript received 12 May 2020, in final form 20 October 2020)

ABSTRACT: Although observational efforts have been made to detect submesoscale currents (submesoscales) in regions with deep mixed layers and/or strong mesoscale kinetic energy (KE), there have been no long-term submesoscale observations in subtropical gyres, which are characterized by moderate values of both mixed layer depths and mesoscale KE. To explore submesoscale dynamics in this oceanic regime, two nested mesoscale- and submesoscale-resolving mooring arrays were deployed in the northwestern Pacific subtropical countercurrent region during 2017–19. Based on the 2 years of data, submesoscales featuring order one Rossby numbers, large vertical velocities (with magnitude of 10–50 m day^{−1}) and vertical heat flux, and strong ageostrophic KE are revealed in the upper 150 m. Although most of the submesoscales are surface intensified, they are found to penetrate far beneath the mixed layer. They are most energetic during strong mesoscale strain periods in the winter–spring season but are generally weak in the summer–autumn season. Energetics analysis suggests that the submesoscales receive KE from potential energy release but lose a portion of it through inverse cascade. Because this KE sink is smaller than the source term, a forward cascade must occur to balance the submesoscale KE budget, for which symmetric instability may be a candidate mechanism. By synthesizing observations and theories, we argue that the submesoscales are generated through a combination of baroclinic instability in the upper mixed and transitional layers and mesoscale strain-induced frontogenesis, among which the former should play a more dominant role in their final generation stage.

KEYWORDS: Subtropics; Eddies; Frontogenesis/frontolysis; Fronts; Oceanic mixed layer; In situ oceanic observations

1. Introduction

Oceanic submesoscale currents (submesoscales for short hereafter) are characterized by order one Rossby and Richardson numbers and have length and time scales $O(0.1\text{--}10)$ km and $O(0.1\text{--}10)$ days at middle latitudes, respectively (Boccaletti et al. 2007; Thomas et al. 2008; Qiu et al. 2014; McWilliams 2016). Due to the above dynamical nature, submesoscales are believed to play significant roles in the following two aspects of oceanography, although their potential importance could be far beyond these. First, as the intermediate scale between mesoscale eddies and small-scale turbulence, the submesoscales can break geostrophic balance and provide an important route for forward energy cascade that dissipates the geostrophic energy (Capet et al. 2008b; D'Asaro et al. 2011; Thomas et al. 2013; Barkan et al. 2015; Gula et al. 2016a). Second, corresponding to their strong ageostrophic motions, submesoscales have large vertical velocity w (Mahadevan and Tandon 2006; Thomas et al. 2008; Brannigan 2016; Yu et al. 2019), which plays a critically important role

in modulating biogeochemical processes as well as the heat budget in the upper ocean (Mahadevan et al. 2012; Mahadevan 2016; Thompson et al. 2016; Su et al. 2018; Taylor 2018; Siegelman et al. 2020). Recognition of the above two important roles makes the submesoscale “mixing” or “transporting” effect an essential aspect that should be parameterized in the present-day eddy-resolving models (with ~ 10 -km horizontal resolution; Fox-Kemper et al. 2008, 2011, 2019; Bachman et al. 2017).

Although the upper-ocean submesoscales had already been discovered by space photography and satellite images in the 1980s (e.g., Flament et al. 1985; Scully-Power 1986), it was only in the 2000s that systematical studies of submesoscales became possible when numerical models and observational techniques began to have the capabilities to partially resolve them (McWilliams 2016, 2019). To investigate spatiotemporal variations of submesoscales, a great number of realistic submesoscale-permitting numerical simulations, with horizontal resolution of $O(1)$ km, were performed in different areas from regional to global scopes (e.g., Capet et al. 2008a; Mensa et al. 2013; Zhong and Bracco 2013; Zhong et al. 2017; Sasaki et al. 2014; Molemaker et al. 2015; Gula et al. 2016b; Barkan et al. 2017; Srinivasan et al. 2017; Su et al. 2018; Qiu et al. 2018; Tedesco et al. 2019; Zhang et al. 2020). These numerical studies generally suggested the following basic dynamical and statistical characteristics of submesoscales: large Rossby number (Ro), strong w , positive

Supplemental information related to this paper is available at the Journals Online website: <https://doi.org/10.1175/JPO-D-20-0100.s1>.

Corresponding authors: Jiwei Tian, tianjw@ouc.edu.cn; Zhiwei Zhang, zzw330@ouc.edu.cn

DOI: 10.1175/JPO-D-20-0100.1

© 2021 American Meteorological Society. For information regarding reuse of this content and general copyright information, consult the AMS Copyright Policy (www.ametsoc.org/PUBSReuseLicenses).

Brought to you by OCEAN UNIVERSITY OF CHINA | Unauthenticated | Downloaded 01/06/21 07:24 AM UTC

skewness of relative vorticity, much stronger in the mixed layer, upward vertical heat flux (VHF), etc. They also suggested that in open oceans away from topography, submesoscales tend to be much stronger in winter corresponding to the seasonality of mixed layer depth (MLD) and are usually strengthened in mesoscale eddy-rich regions due to the strong strain field.

Compared with numerical simulations, due to their small spatial scale and rapid evolution, directly observing submesoscales in the ocean is more challenging. Until now, there are only a limited number of submesoscale field experiments that have been conducted, including LatMix¹ and OSMOSIS² in the North Atlantic (Shcherbina et al. 2015; Klymak et al. 2016; Buckingham et al. 2016; Erickson et al. 2020), GLAD³ and LASER⁴ in the Gulf of Mexico (Poje et al. 2014; D'Asaro et al. 2018), SMILES⁵ in the Southern Ocean (Adams et al. 2017), and also several other submesoscale targeted cruises in different regions (e.g., D'Asaro et al. 2011; Zhang et al. 2016; Pascual et al. 2017; Naveira Garabato et al. 2019). The high-resolution data were successfully used to estimate relative vorticity, w , potential vorticity (PV), VHF, and other quantities associated with submesoscales, which generally confirmed the spatiotemporal characteristics of submesoscales simulated by numerical models. Particularly, several of these observational studies demonstrated that the positive VHF induced by submesoscales is comparable in magnitude to the net surface heat flux, highlighting the important role of submesoscales in modulating the upper-ocean heat budget (Thompson et al. 2016; Yu et al. 2019). Based on these observed characteristics, it is argued that in the open ocean, mixed layer instability (MLI) and strain-induced frontogenesis are likely two most important mechanisms responsible for the submesoscale generations (Callies et al. 2015; Siegelman et al. 2020), which are consistent with the earlier quasigeostrophic theories and idealized numerical simulations (Lapeyre et al. 2006; Boccaletti et al. 2007). However, which mechanism (MLI or frontogenesis) is more dominant seems to be situation dependent, and it is difficult to determine based on data because the two mechanisms usually co-occur in the real ocean (McWilliams 2016; Srinivasan et al. 2017).

Despite the above submesoscale experiments made in the ocean, except for the OSMOSIS mooring array that has obtained yearlong time series at fixed locations, all of the other experiments were heavily based on shipboard instruments [e.g., acoustic Doppler current profiler (ADCP) and conductivity–temperature–depth (CTD)] or autonomous platforms (e.g., gliders, floats, drifters) and thus only provided short-term (or snapshot) and time-discontinuous observations. The problem of these short-term observations lies in its difficulty to separate the submesoscales and internal waves that have overlaps in their spatial and time scales, which can bring large uncertainties when inferring the submesoscale quantities (Rocha et al. 2016; Torres et al. 2018; Qiu et al. 2018; Cao et al. 2019). In addition, most of

the previous experiments were conducted at the mid-to-high latitudes (higher than $\sim 30^\circ\text{N/S}$) and dynamically, their locations are featured by deep wintertime mixed layer due to strong cooling or/and strong mesoscale eddy kinetic energy (EKE) corresponding to the western boundary currents or the Antarctic Circumpolar Current (ACC). In contrast, the submesoscale observations within the lower-latitude subtropical gyre are rare. Compared with the existing experimental locations, the lower-latitude subtropical gyre has both moderate EKE (thus mesoscale strains) and wintertime MLD (Chelton et al. 2011; Holte et al. 2017). Because the generation of submesoscales strongly depends on mesoscale strains and MLD (McWilliams 2016), it will improve our knowledge of submesoscales if a long-term field experiment is conducted in such a different dynamical regime (i.e., the subtropical gyre).

Here, we report the first long-term submesoscale observations in the North Pacific Subtropical Countercurrent (STCC; Fig. 1), a common phenomenon in the global subtropical gyres featured by moderate values of both EKE and winter MLD (Tomczak and Godfrey 2003; Talley 2011). In contrast to the region of OSMOSIS, the only long-term experiment so far, the STCC region focused on here has shallower MLD but much larger EKE.⁶ In addition, due to the lower latitude of our study region, the inertial frequency here is less than a half of the OSMOSIS region. It should be noted that due to the seasonal variation of baroclinic instability intensity associated with the STCC, the EKE shows a seasonal cycle opposite to that of the MLD and reaches the peak and trough in June and January, respectively (Fig. S1 in the online supplemental material; Qiu 1999). The opposite seasonality between EKE and MLD in the North Pacific STCC (also true for the other STCCs; see, e.g., Qiu and Chen 2004; Jia et al. 2011) makes it a good testing ground to investigate the generation dynamics of submesoscales (i.e., frontogenesis versus MLI) if their seasonal variation is revealed. To this end, two nested mooring arrays (one mesoscale- and one submesoscale-resolving) similar to the OSMOSIS were deployed for 2 years in the northwestern Pacific STCC. Based on these long-term moored data, dynamical features and mechanisms of the submesoscales are investigated in this study. The remainder of this paper is organized as follows. Section 2 introduces the data and methods we used. Section 3 presents the results including basic dynamical quantities, temporal modulations, and energetics of the submesoscales. In section 4, generation mechanisms of the submesoscales, their impact on the upper-ocean heat budget, as well as their seasonality are discussed. Finally, the conclusions are given in section 5.

2. Data and methods

a. Observational experiment

To study the scale–scale interactions and energy cascade among mesoscale eddies, submesoscale currents, and internal waves in the subtropical northwestern Pacific, the Subtropical

¹ Scalable Lateral Mixing and Coherent Turbulence.

² Ocean Surface Mixing, Ocean Submesoscale Interaction Study.

³ Grand Lagrangian Deployment Experiment.

⁴ Lagrangian Submesoscale Experiment.

⁵ Surface Mixed Layer Evolution at Submesoscales.

⁶ Based on long-term historical altimeter data, the spatial mean EKE within an $8^\circ \times 8^\circ$ box is ~ 5 times of that in the OSMOSIS region.

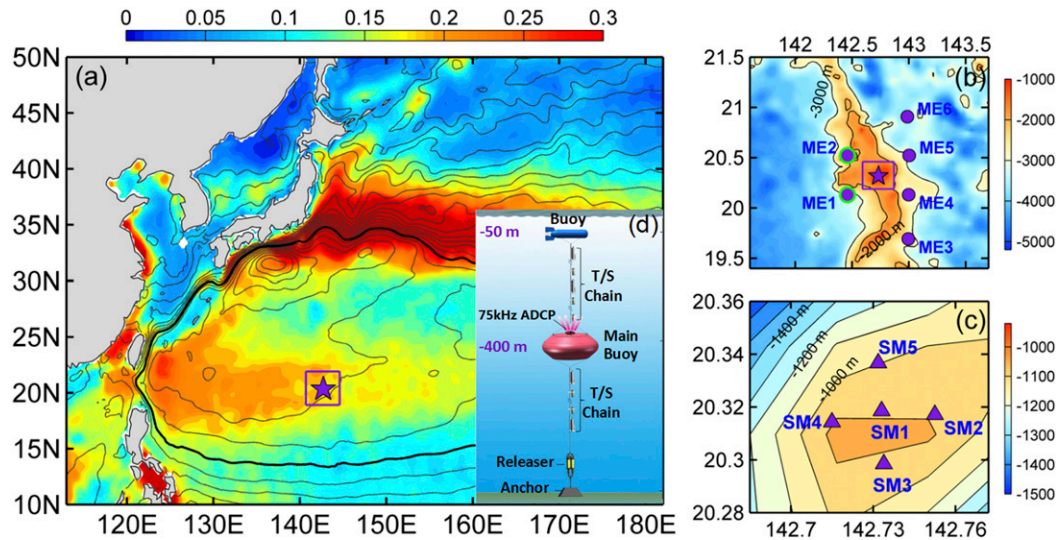


FIG. 1. (a) Distribution of the mean \sqrt{EKE} in the northwestern Pacific (color shading; $m s^{-1}$) and the rough location of the SubMESI mooring arrays (purple square and star). Gray lines are the contours of mean sea surface height (SSH) with an interval of 8 cm, among which the 120-cm SSH contour is highlighted using black thick line. Both the mean EKE and SSH are obtained from the merged satellite altimeter product between 1993 and 2017. (b) Bathymetry (color shading; m) and mooring locations in the experimental region. Purple dots and star denote the ME and SM moorings, respectively. (c) Zoom in on the purple square in (b). Locations of the SM moorings are denoted by purple triangles. (d) Schematic diagram of the configuration of a typical SM mooring. Names of the instruments are marked in the diagram. Depths of the topmost and the main buoys are also marked.

Mesoscale, Submesoscale, and Internal waves (SubMESI) experiment was conducted during 2017–19. This experiment was partially motivated by the previous Northwestern Pacific Eddies, Internal waves and Mixing Experiment (NPEIM) observations, which revealed that interaction between mesoscale eddies and near-inertial waves strongly elevated the diapycnal mixing in the North Pacific STCC (Zhang et al. 2018). However, the NPEIM experiment failed to address the role of submesoscales due to the relatively coarse observational resolution. To obtain long-term and continuous observations that can concurrently capture the mesoscale eddies, the internal waves and, most importantly, the submesoscales, two mooring arrays with one mesoscale resolving and the other submesoscale resolving were deployed in the northwestern Pacific STCC region of 142°–143°E, 19°–22°N between March 2017 and March 2019 (Fig. 1a). The two arrays are nested in space with the design similar to OSMOSIS, but the deployments and instrument configurations of the moorings are different and have some improvements compared with OSMOSIS in the following aspects.

First, the SubMESI moorings were maintained for ~ 2 years with three deployment–recovery cycles (by four cruises). Observational periods of the three cycles are March–December 2017, December 2017–April 2018, and April 2018–March 2019, respectively. During the first cycle, eight mesoscale moorings were deployed along $\sim 143^\circ E$ between 18.9° and $21.8^\circ N$ and five submesoscale moorings with a cross shape were deployed centered on $20.3^\circ N$, $142.7^\circ E$. The mesoscale and submesoscale mooring arrays (ME and SM arrays hereafter) have the horizontal spacing of 30–40 km and ~ 2 km, respectively. For the

second and third observational cycles, their mooring locations are the same; compared with the first cycle, the SM array and the central four moorings of the ME array remained and two new ME moorings were deployed west of the SM array along $\sim 142.5^\circ E$ (Figs. 1b,c). Because the first baroclinic deformation radius and wintertime mixed layer deformation radius in the STCC region are 50–60 km (Chelton et al. 1998) and ~ 3 km (calculated using NH/f , where H is the MLD, f is the Coriolis parameter, and N is the averaged stratification within the mixed layer defined as 0.03 kg m^{-3} potential density difference relative to sea surface), respectively, the SubMESI arrays can to a large degree resolve the typical mesoscale eddies and wintertime submesoscales here.

Second, all the ME (SM) moorings are equipped with one upward- and one downward-looking (one upward-looking) 75-kHz RDI ADCPs at ~ 400 -m depth to observe the current velocity in the upper ~ 900 m (~ 400 m) every half or an hour; all of the moorings are also equipped with temperature chains, consisting of several CTDs and dozens of Seabird temperature loggers, to measure the temperature/salinity (T/S) in the upper ~ 800 – 1000 m every 3–10 min (Fig. 1d, Tables S1 and S2). In addition to measuring T/S , another important aim of the moored CTDs is to provide the depth information for the temperature chain. The uppermost instrument is just beneath the top float that is on average ~ 50 m beneath sea surface, where the influence of wind waves and swell is small. For the ADCPs on the SM (ME) moorings, they have a vertical sampling interval of 8 m (16 m), while for the temperature chains, their vertical resolutions are 10, 20, and 40 m above the 200 m, between 200–400 m and 400–800 m (10–20 and 50 m above

and below ~ 500 m), respectively. These vertical resolutions are much higher than the current meter/CTD pairs used on the OSMOSIS moorings (e.g., Yu et al. 2019), which can greatly reduce the uncertainties caused by vertical interpolations, especially when calculating differentials of velocity or temperature between two moorings. In addition, the ME moorings are also equipped with one or two current meter–CTD pairs at ~ 2000 and 3000 m to measure the velocity and T/S in the deep ocean (not used in this study).

Third, in contrast to the deep water of the OSMOSIS site (depth of ~ 4800 m), the SM moorings were deployed on top of a shallow ridge, whose averaged water depth is only ~ 1000 m (Fig. 1c). In addition, compared with our previous regular moorings (e.g., those in Zhang et al. 2018), more buoyancy was added to the main floating body of the SubMESI moorings. The above designs greatly reduced the vertical and horizontal excursions of the moorings, even during strong-current events. During the 2-yr observational period, only for 0.11% (0.10%) of the time does the pitch (roll) of ADCPs exceed 15° , the maximum measuring range of the tilt sensor; the percentage of large ADCP fall-off depths exceeding 30 m is only 0.37% (i.e., 2.7 days for time length). The maximum velocity errors caused by the tilt and horizontal swing of ADCPs are $O(10^{-4})$ m s^{-1} and $O(10^{-4}\text{--}10^{-3})$ m s^{-1} , respectively, which are from two to four orders smaller than the typical mesoscale and submesoscale velocities focused on here (see the details in appendix A). Furthermore, the small horizontal excursions ensured that the mooring positions and the horizontal distances among the moorings did not change much, which is vitally important to calculate gradients of the quantities involving space differential. According to the evaluation in appendix A, the relative error of vertical vorticity caused by the uncertainty of mooring positions is no more than 6%.

The detailed configuration and instrumental information for each mooring are shown in Tables S1 and S2. During the 2-yr-long experiment period, except for the SM1 mooring (i.e., central mooring of the SM array) that was kept onsite for the third observational cycle, all of the other moorings were successfully recovered. In addition, due to the cable break, the temperature loggers between 80 and 200 m on the SM4 mooring were lost in the third cycle. Similar temperature chain loss also occurred above 290 m for the ME3 in the first cycle and above 260 m for the ME4 during the whole period. Overall, all the recovered ADCPs and temperature chains functioned well, and they provided us 2-yr-long high-quality continuous velocity and temperature profiles (only 1 year for SM1).

b. Data processing

Before detailed analysis, the raw moored data were first processed using a standard procedure as in our earlier mooring-based studies (e.g., Zhang et al. 2015a, 2016). Specifically, the original high-frequency velocity and temperature data were first hourly averaged. Then, the hourly data were linearly interpolated onto uniform 10 m vertical levels between near surface (20–50 m) and the ~ 900 -m (or ~ 400 -m) depth. Although the submesoscales also contain some energy in the superinertial time scale, we focused in this study on their subinertial components because the superinertial ones are entangled with internal

waves that are difficult to separate cleanly (e.g., Qiu et al. 2018). To remove the internal-wave signals, a 2-day low-pass filter (fourth-order Butterworth) was therefore applied to the hourly time series (the inertial period at the SM array is ~ 1.4 days). After that, the low-pass-filtered data were further daily averaged. The daily velocity and temperature data from the SM array (Fig. 2) and velocity data from the ME array (ME3–ME6 in the first cycle) were finally used in the following analyses.

c. Calculation of relative vorticity

Vertical component of the relative vorticity ζ is calculated using the SM array in the following two ways. The first way follows the definition $\zeta = \partial v/\partial x - \partial u/\partial y$, where u and v are the zonal and meridional velocity, respectively. In practice, it is estimated using $\Delta v/\Delta x - \Delta u/\Delta y \approx (v_2 - v_4)/(x_2 - x_4) - (u_5 - u_3)/(y_5 - y_3)$, where the subscript denotes the SM mooring number (see Fig. 1c). The second way is through the Stokes theorem as used in Buckingham et al. (2016), i.e., $\zeta = 1/A \oint \mathbf{v} \cdot d\mathbf{l}$. In the practical calculation, the line integral is along the square composed of the outer four moorings (i.e., SM2–SM5 in Fig. 1c), A is the area of this square, and $d\mathbf{l}$ and \mathbf{v} are the distance vector and averaged velocity of two neighbor moorings, respectively. The results derived from the two ways are nearly the same, demonstrating the robustness of the estimated ζ .

d. Calculation of vertical velocity

Theoretically, both the continuity equation and the density equation can be applied to the mooring-array data to estimate w . However, given that no reliable reference level of w_0 is available for $w = w_0 + \int_{z_0}^z (\partial u/\partial x + \partial v/\partial y) dz$ (note that because the ADCPs failed to give data in the upper ~ 50 m, the rigid-lid assumption cannot be applied), the continuity equation method is therefore abandoned. Alternatively, the density conservative equation that neglects the turbulent diffusion terms (not available in our observations) in the density equation is used here:

$$\frac{D\rho}{Dt} = \frac{\partial \rho}{\partial t} + u \frac{\partial \rho}{\partial x} + v \frac{\partial \rho}{\partial y} + w \frac{\partial \rho}{\partial z} = 0, \quad (1)$$

where ρ is the potential density. This method has recently been successfully applied to the OSMOSIS data, and it was demonstrated to have a good capability to properly estimate w beneath the surface mixed layer (Yu et al. 2019). Because the salinity measurements from CTD are coarse on our moorings, the potential temperature conservative equation is used instead with w given by

$$w = - \frac{\left(\frac{\partial T}{\partial t} + u \frac{\partial T}{\partial x} + v \frac{\partial T}{\partial y} \right)}{\frac{\partial T}{\partial z}}, \quad (2)$$

where T is the potential temperature referenced to sea surface. To calculate w , the u , v , $\partial T/\partial t$, and $\partial T/\partial z$ are obtained from the central-mooring measurements (i.e., SM1), and $\partial T/\partial x$ and $\partial T/\partial y$ are computed using the mooring pairs (SM2, SM4) and (SM3, SM5), respectively. Because the mooring SM1 was not

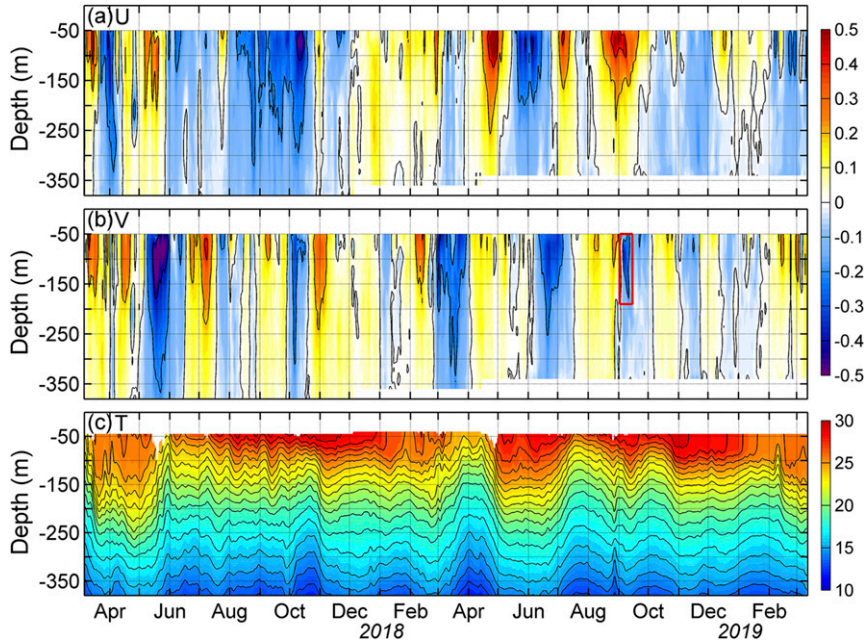


FIG. 2. Depth–time plots of the subinertial (a) zonal velocity, (b) meridional velocity, and (c) temperature averaged among the SM moorings. Black lines in (a), (b), and (c) are contours of velocity and temperature, respectively, with the respective intervals of 0.2 m s^{-1} and 1°C . The red rectangle in (b) indicates the typhoon-related submesoscale event. Irregular blanks in (c) are due to excursions of the moorings.

recovered for the second year (the third observational cycle), we estimate w only for the first year.

e. Calculation of geostrophic and ageostrophic velocity

Geostrophic velocity u_g and v_g at the SM array are calculated based on the thermal wind relations:

$$u_g = u_0 + \int_{z_0}^z \frac{g}{\rho_0 f} \frac{\partial \rho}{\partial y} dz, \quad (3)$$

$$v_g = v_0 - \int_{z_0}^z \frac{g}{\rho_0 f} \frac{\partial \rho}{\partial x} dz. \quad (4)$$

In the above formulas, $g = 9.8 \text{ m s}^{-2}$ is the gravity acceleration, $\rho_0 = 1025 \text{ kg m}^{-3}$ is the referenced density, f is the Coriolis parameter, z_0 is the reference level, and u_0 and v_0 are the zonal and meridional velocity at the reference level, respectively. Here, instead of the commonly used zero-velocity assumption at a deep layer, we use the SM-array averaged ADCP velocity at -360 m (i.e., z_0) as a referenced velocity (i.e., u_0 and v_0) in (3) and (4). The potential density ρ is computed using the MATLAB SeaWater toolbox (<http://www.cmar.csiro.au/datacentre/>) by combining the mooring-observed temperature and the IPRC monthly Argo-derived salinity data (<http://apdrc.soest.hawaii.edu/>; see also Zhang et al. 2018). The way to calculate $\partial \rho / \partial x$ and $\partial \rho / \partial y$ is the same as with $\partial T / \partial x$ and $\partial T / \partial y$ mentioned above. After calculating the geostrophic velocity, the ageostrophic velocity (u_a and v_a) can be obtained by subtracting the geostrophic velocity from the ADCP velocity. Given that the SM1 mooring was not recovered and the upper

200-m temperature chains on the SM4 mooring were lost during the second year, we calculate the geostrophic and ageostrophic velocities only for the first year.

f. Calculation of mesoscale strain rate

The ADCP velocity data from the ME moorings combined with the SM array-averaged velocity are used to calculate the mesoscale strain rate (MSR). The MSR is defined as

$$\text{MSR} = \sqrt{\left(\frac{\partial u_m}{\partial x} - \frac{\partial v_m}{\partial y}\right)^2 + \left(\frac{\partial u_m}{\partial y} + \frac{\partial v_m}{\partial x}\right)^2}, \quad (5)$$

where, u_m and v_m denote mesoscale velocities calculated using a 15-day low-pass filter. For the first observation cycle, MSR is calculated based on the triangle made up of the moorings SM1, ME4, and ME5 (due to the absence of the moorings ME1 and ME2). For the second and third observational cycles, the four triangles made up of SM1 and the four ME mooring pairs (i.e., ME1–ME2, ME1–ME4, ME4–ME5, and ME5–ME2) are independently used to calculate MSR, and their averaged result is adopted. The detailed procedure on how to calculate MSR from three points in a triangle can be found in appendix B.

g. Calculation of mixed layer depth

The SM-array averaged temperature is used to calculate MLD. Here, MLD is defined as the depth where temperature is 0.1°C lower than the uppermost temperature at $\sim 40 \text{ m}$ depth. This temperature threshold is chosen because by analyzing all

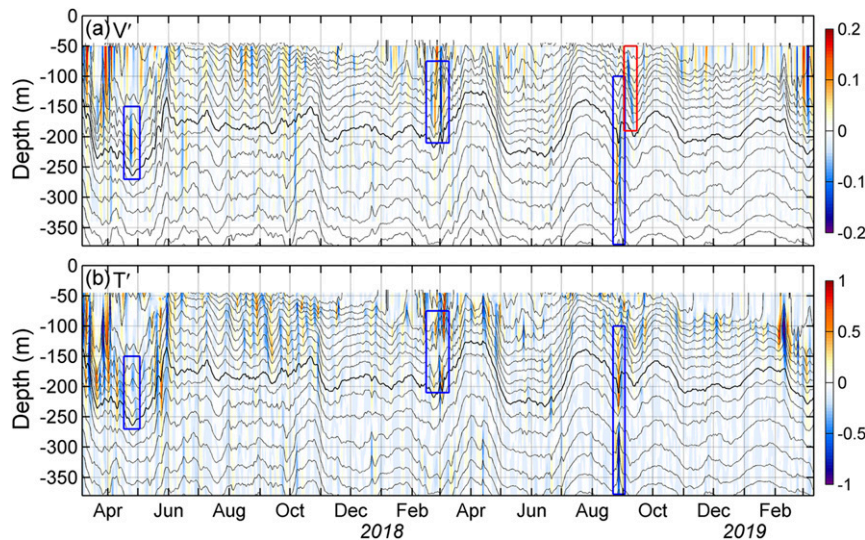


FIG. 3. (a),(b) As in Figs. 2b and 2c, respectively, but for the 15-day high-pass-filtered anomalies (color shading). Black lines are the temperature contours with an interval of 1°C , among which the 20°C contour is highlighted by thick line. Blue and red rectangles indicate the occurrence of the SCVs and the typhoon-related submesoscale event, respectively.

the historical Argo profiles near the SM array (within a $3^{\circ} \times 3^{\circ}$ box) during the 2-yr observational period, the calculated MLD based on our definition has the minimum root-mean-square error when compared with the result calculated using the commonly adopted 0.2°C threshold relative to the sea surface (de Boyer Montégut et al. 2004). Note that because the mixed layer is shallower than the uppermost moored measurement in summer, the MLD calculation is only performed from late autumn to early spring. In addition, MLD is also calculated based on the daily temperature data of the $1/12^{\circ}$ Hybrid Coordinate Ocean Model (HYCOM) global reanalysis product using the 0.2°C threshold. The HYCOM product has assimilated multiple observational data, including satellite sea surface height and temperature data, Argo float data, moored and shipboard T/S and velocity data, and so on. Owing to the data assimilation, the depth–time distribution of the HYCOM temperature shows a good agreement with the moored temperature (Fig. S2), suggesting that HYCOM can to a large degree reproduce the MLD variations in our study region. The overall consistency between the moored- and HYCOM-derived MLDs between October and March supports this notion (Fig. S2, Fig. 4).

3. Results

a. Moored velocity and temperature

In Fig. 2, we show the depth–time plots of the subinertial daily velocity and temperature derived from the SM array. The most remarkable phenomenon at first glance is the mesoscale eddies, which show strong velocities (as large as 0.5 m s^{-1}) and thermocline fluctuations (amplitude as large as 100 m) with a period of ~ 3 months. This period agrees roughly with the previous observations and is attributable to the westward propagation of mesoscale eddies generated by baroclinic instability

associated with the STCC (Qiu 1999; Zhang et al. 2001; Lien et al. 2014). Although the mesoscale eddies are generally surface intensified, their signals can reach to more than 2000 m (from the ME data, figure not shown). The 2-yr-long time series also show that most of the strong mesoscale signals occur between April and October, which agrees with the seasonality of altimeter-derived EKE revealed by previous studies (Qiu 1999; Qiu et al. 2014).

Accompanying the lower-frequency mesoscale eddies, there are smaller-scale signals with the period shorter than 15 days. These short-period processes become more evident after we applied a 15-day high-pass filter to the velocity and temperature time series (Fig. 3). In contrast to the mesoscale eddies, these processes primarily occur in late winter and early spring (February–April); they have much smaller vertical scales, and their energy is mainly confined to the upper ~ 150 m. In addition, the magnitudes of their velocity and temperature anomalies are only 0.1 m s^{-1} and 1°C , respectively, much smaller than the mesoscale eddies (i.e., 0.5 m s^{-1} and 5°C). There are also three exceptional events with large velocity or temperature anomalies beneath 150 m. Two of them are associated with lens-like structures (seen from the isotherms distribution) with their centers between 150 and 250 m in late April 2017 and between 100 and 200 m in late February and early March 2018, respectively. The third event is associated with a prism-like structure occurring between 100 and 400 m in late August 2018. The abovementioned shorter-period processes are the submesoscales of the focus of this study. Their detailed characteristics and mechanisms are investigated below.

b. Rossby number

Figure 4 shows the 2-yr-long depth–time distribution of Ro (i.e., ζ/f) derived from the SM array. In contrast to the velocity and temperature, the variation of Ro is primarily dominated by

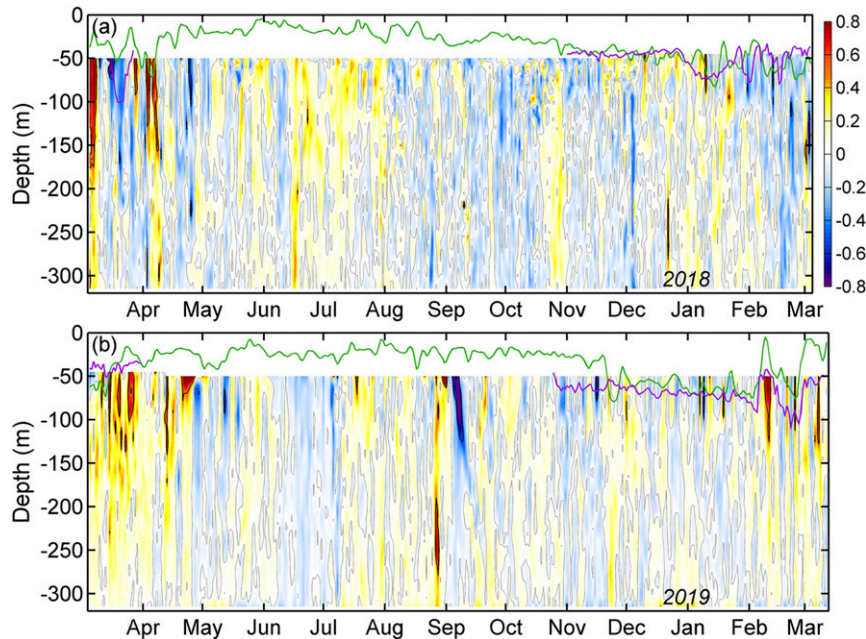


FIG. 4. Depth–time plots of the Rossby number (i.e., $Ro = \zeta/f$) between (a) March 2017 and March 2018 and (b) March 2018 and March 2019. The zero and ± 0.5 contours of the Rossby number are indicated by gray and black lines, respectively. Purple and green lines denote the MLD calculated using the moored and HYCOM temperature, respectively.

the shorter-period processes (period < 15 days) rather than the energy-containing mesoscale eddies. At the time and depths where large shorter-period velocity/temperature anomalies occur (Fig. 3), Ro also shows large values with magnitude exceeding 0.5 (sometimes exceeding 1.0), suggesting the submesoscale nature of these shorter-period processes. Except for the lens- and prism-like structures that show subsurface-intensified Ro , the large values of Ro mainly occur in the upper ~ 150 -m layer. Corresponding to the lens- and prism-like structures, Ro shows large negative and positive values, respectively. They are essentially anticyclonic and cyclonic submesoscale coherent vortices (SCVs; McWilliams 1985) but are not the focus of this study. Although the submesoscale Ro generally decreases with depth (with the exception for the SCVs), its large values can actually penetrate far beneath the base of the mixed layer. In many cases, the ± 0.5 isoline of Ro can reach 150 m, much deeper than the MLD that is on average only 70–80 m in winter. Seasonally, the large Ro values (magnitude larger than 0.5, hereafter) primarily occur between January and April. However, a significant exception is found in early September 2018, when the negative Ro was found to be lower than -1.0 . This strong submesoscale event presents a clear downward propagating tendency, which can also be seen from the depth–time plots of velocity (Figs. 2b and 3a). It is associated with the breaking of downward-propagating near-inertial internal waves generated by a strong typhoon at that time, which severely perturbed the thermocline. This special submesoscale event is also not focused on here and we will investigate its mechanism in detail in a future study.

The abovementioned vertical distribution and seasonality of Ro can also be seen from the probability density function (PDF) of Ro at different depths (Fig. 5). For the upper layer at 70 m, 15% of the absolute Ro values are larger than 0.5 in the winter–spring season (January–April, hereafter), while the percentage is only 1% in the summer–autumn season (June–October, hereafter). In the winter–spring season, the PDF of Ro displays a significant asymmetry with a long tail for large positive values, and the percentages of $Ro > 0.5$ and $Ro < -0.5$ are 11% and 4%, respectively. Corresponding to this asymmetry, the Ro shows a large positive skewness in the upper 100 m in the winter–spring season (Fig. S3). The above seasonality and asymmetry of submesoscales are generally consistent with those found by previous observations (Shcherbina et al. 2013; Callies et al. 2015; Buckingham et al. 2016; Qiu et al. 2017). With respect to the deeper layer at 200 m, the PDF of Ro is much thinner and taller, and both the seasonality and asymmetry found at the 70-m layer disappear. At this depth, 98% of the absolute Ro values are smaller than (or equal to) 0.3, demonstrating that the motions here are dominated by quasigeostrophic mesoscale eddies.

In Fig. 6, we show the power spectra of ζ and velocity averaged between 50 and 100 m. It is found that in the winter–spring season, the spectrum of ζ exhibits strong energy peaks at the periods between 4 and 14 days (Fig. 6a). In contrast, power spectrum density of the ζ is dominated by mesoscale motions with period longer than 15 days in the summer–autumn season. The two spectra have an intersection at the period of ~ 14 days. These results, on one hand, further demonstrate the distinct seasonalities of submesoscales and mesoscale eddies and, on

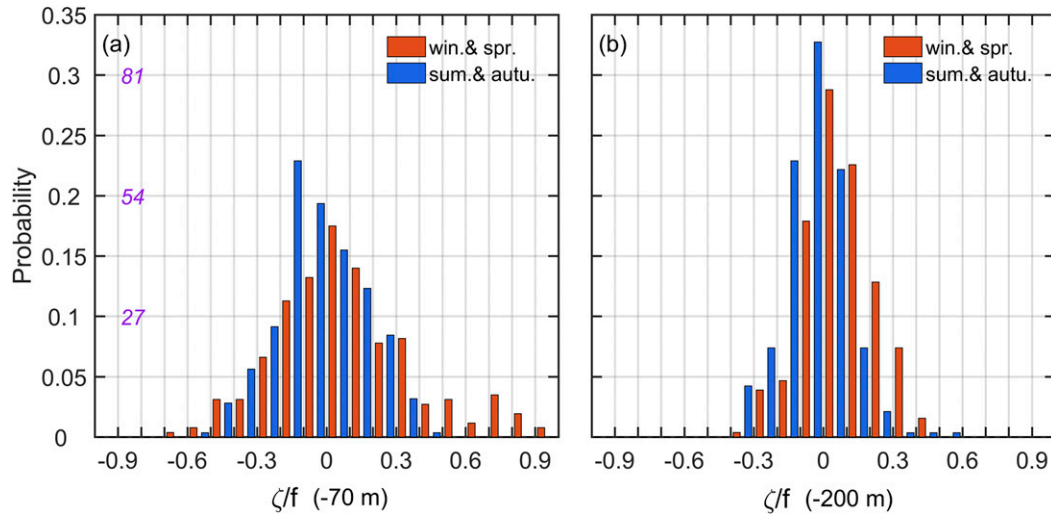


FIG. 5. Probability density distribution of the Ro at the (a) 70- and (b) 200-m depths. The results in the winter-spring and summer-autumn seasons are indicated by red and blue histograms, respectively. Note that the typhoon-related submesoscale event in September 2018 is excluded in the statistics. The numbers of points corresponding to the probabilities of 0.1, 0.2, and 0.3 are marked on the y axis of (a).

the other hand, indicate that the 15 days is a reasonable time scale to distinguish the mesoscale and submesoscale motions. Different from the mooring-derived results, the spectrum of ζ computed based on the gridded altimeter data fails to capture the submesoscale signals and its energy density is from one to two orders smaller than the moored results. This is understandable because the present-day altimeter product can only resolve motions with wavelengths larger than 150 km (Fu et al. 2010). Similarly, the spectrum of velocity in the winter-spring season also shows elevated energy between 4 and 10 days and the spectra in two seasons also intersect at ~ 14 days (Fig. 6b).

The difference is that, compared with the ζ spectrum, the velocity spectrum is generally redder and, even in the winter-spring season, the energy in the submesoscale band is lower than the mesoscale band. This is consistent with the results in Figs. 2a, 2b, and 3a that the horizontal velocity of submesoscales is much weaker than mesoscale eddies.

c. Vertical velocity

The vertical velocity w inferred from the SM mooring array based on density conservative equation is shown in Fig. 7a. Generally, w displays vertical and temporal variations very

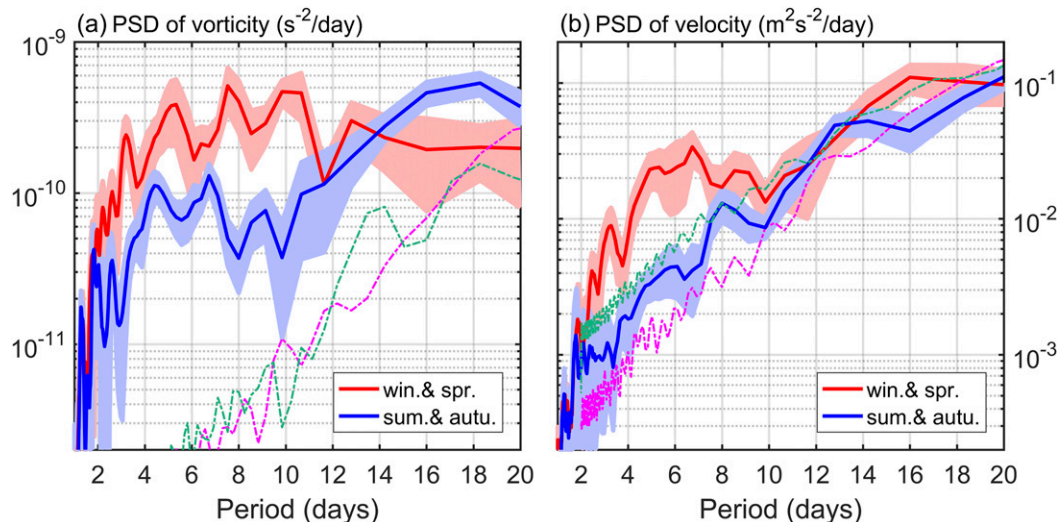


FIG. 6. Upper-layer averaged (between 50 and 100 m) power spectra of (a) relative vorticity and (b) horizontal velocity. The red and blue solid (pink and green dashed) lines denote the mooring-derived (altimeter-derived) results in the winter-spring and summer-autumn seasons, respectively. The red and blue shadings denote the 95% confidence intervals of the solid lines calculated using bootstrap method.

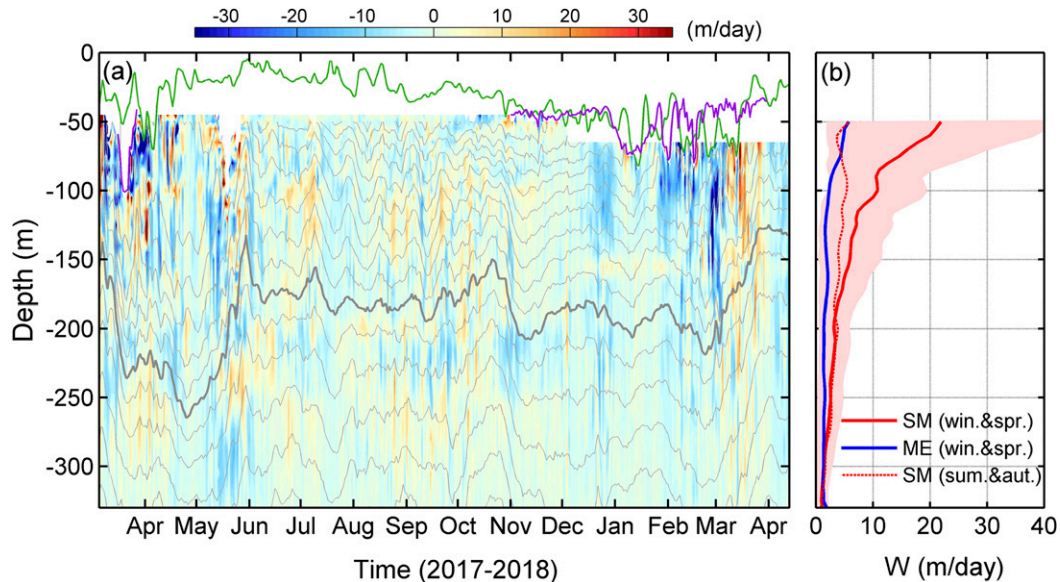


FIG. 7. (a) Depth–time plot of the vertical velocity (color shading; m day^{-1}). Purple and green lines denote mooring- and HYCOM-derived MLD, respectively. Gray lines are temperature contours with an interval of 1°C and the gray thick line indicates the 20°C contour. (b) Vertical profiles of the seasonal mean $|w|$. Red and blue solid lines are the results for the submesoscale and mesoscale w in the winter–spring season, respectively. The result for the submesoscale w in the summer–autumn season is indicated by red dashed line. Red shading denotes the standard deviation associated with the red solid line.

similar to Ro. Specifically, large w values primarily occur in the upper ~ 150 m and in the winter–spring season. The strongest w occurred in late March and early April 2017, whose magnitude exceeded 50 m day^{-1} . Averaged across the 50–100-m layer, the root-mean-square w values in the winter–spring and summer–autumn seasons are 19.8 and 4.8 m day^{-1} , respectively. It should be noted that compared with the positive w , the negative ones happen more frequently and have larger magnitudes, especially in the winter–spring season. In other words, the vertical motions are dominated by downwellings, which can also be seen from the PDF of w between the 50- and 100-m layers (Fig. S4a). This is consistent with the positive skewness of Ro because from the PV conservation, development of positive ζ in the upper layer requires the water column to stretch through subsurface downwelling (Capet et al. 2008a). The ageostrophic advective feedback on the secondary circulation during frontogenesis may also play a role in the negative skewness of w found here (McWilliams 2016). Corresponding to the dominantly downward w that decreases with depth below 50 m (i.e., $\partial w/\partial z < 0$), the horizontal divergence (i.e., $\partial u/\partial x + \partial v/\partial y$) is dominated by positive values between 50 and 100 m (Fig. S4b). Predominantly convergent flows are expected above 50 m, whose presence, however, is beyond the observational range by the ADCPs.

If we separate w into mesoscale and submesoscale components using the 15-day low- and high-pass filters, respectively, it is found that w is mainly caused by submesoscales (Fig. 7b), similar to the result of ζ . For the submesoscale w , the time-mean and 50–100-m depth-averaged magnitude reaches 15.2 m day^{-1} (RMS value 21.9 m day^{-1}) in the winter–spring season, which is

much larger than 4.0 m day^{-1} (RMS value 5.6 m day^{-1}) for the mesoscale w in the same season and 4.8 m day^{-1} (RMS value 6.2 m day^{-1}) for the submesoscale w in the summer–autumn season. The submesoscale w inferred here is several times smaller than the OSMOSIS result (Yu et al. 2019), which may be ascribed to the much weaker stratification in the higher-latitude OSMOSIS site. With respect to the mesoscale w , it has a magnitude similar to the previously diagnosed results for the subtropical mesoscale eddies (e.g., McGillicuddy et al. 2007; McGillicuddy 2016; Hu et al. 2011). The relatively weaker w for mesoscale eddies (compared with submesoscales) is reasonable because they are governed by quasigeostrophic dynamics and have weak horizontal divergence. It is worth pointing out that in the winter–spring season, the standard deviation of the submesoscale w is comparable to its mean magnitude, indicating that the observed submesoscales have a strong intraseasonal variation. It will be shown in the following that this variation is closely associated with the mesoscale eddies. Although the intensity of w gradually decreases with depth below 50 m, the seasonally contrasting feature is still evident at ~ 150 m, which agrees with the vertical distribution of ζ and suggests the deep penetration of submesoscales. Because the strong submesoscale vertical motions can penetrate into the nutricline that is between 100 and 150 m in the North Pacific STCC region (e.g., Huang and Xu 2018; Xiu and Chai 2020), they may play an important role in sustaining the phytoplankton growth by transporting subsurface nutrients vertically into the euphotic zone (Lévy et al. 2018), especially in the oligotrophic low-latitude subtropical ocean where the wintertime MLD is shallower than the nutricline.

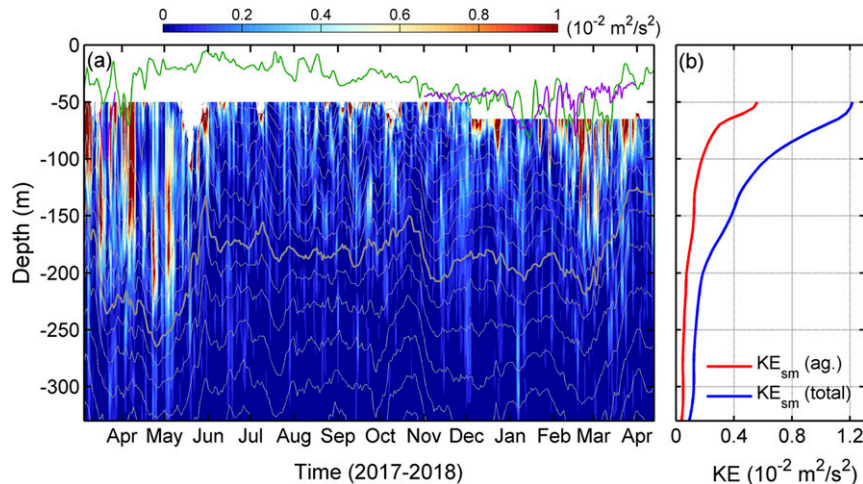


FIG. 8. (a) As in Fig. 7a, but for the ageostrophic KE. (b) Mean profiles of the submesoscale total KE (blue line) and submesoscale ageostrophic KE (red line) in the winter–spring season.

To interpret the depth–time variation of w , ageostrophic kinetic energy [$KE_a = (u_a^2 + v_a^2)/2$] is calculated using the ageostrophic velocity \mathbf{v}_a (method in section 2e; Fig. 8a). Overall, both the vertical and time variations of KE_a have a good correspondence to w , agreeing with the theoretical expectation that it is the ageostrophic current with strong horizontal divergence that generates vertical motions in the ocean. Similar to w and ζ , KE_a is also dominated by submesoscales. After applying a 15-day high-pass (low-pass) filter to the geostrophic and ageostrophic velocities, we then calculated the geostrophic KE and KE_a of submesoscale (mesoscale) motions, respectively. By comparing the submesoscale KE_a with the total submesoscale KE, we found that in the winter–spring season, its contribution can on average reach 35% in the upper 50–100-m layer (Fig. 8b). The mesoscale KE_a , on the other hand, only accounts for 6% of the total mesoscale KE for the same season and depths (figure not shown). We should note that the submesoscales focused on here have totally excluded the superinertial motions. If the superinertial submesoscales are considered, the percentage of KE_a (and also w) would be even higher (D’Asaro et al. 2018). The above quantitative results suggest that although geostrophic balance is a good approximation for mesoscale eddies, it should be careful to apply it to submesoscales, for which the ageostrophic effect cannot be neglected.

d. Temporal modulations of submesoscales

Because the submesoscales are characterized by large Ro, the Ro squared [i.e., $(\zeta/f)^2$], which is the normalized enstrophy in physics, is used here as an index to indicate the strength of submesoscales. To examine the temporal modulations of submesoscales, a 15-day high-pass filter is applied to Ro before calculating the square (recall Fig. 6). In Fig. 9, we show the 2-yr-long time series of the submesoscale enstrophy averaged between 50 and 100 m. The submesoscale enstrophy displays strong intraseasonal modulations with periods ranging from 15 to 45 days. By examining the whole 2-yr-long series, we also

find that these intraseasonal signals are intensified in the winter–spring season (except for the special event in September 2018). The intraseasonal modulations of submesoscales seem to be associated with the mesoscale strain field and the correlation coefficient (r) between the enstrophy and the MSR time series reaches 0.42 in the winter–spring season (exceeding the 95% confidence level, Fig. 9a). Although previous simulation studies suggested that temporal variation of submesoscales is strongly modulated by the MLD (e.g., Mensa et al. 2013; Sasaki et al. 2014), we fail to see a significant correlation between the enstrophy and the MLD in our observations ($r = 0.20$, Fig. 9b). However, an improved negative correlation is found between the enstrophy and the time derivative of MLD ($r = -0.35$, Fig. S5), which may suggest that generation of the submesoscales could have possibly caused restratification that shoaled the mixed layer (e.g., Mahadevan et al. 2012; du Plessis et al. 2017).

To focus on the seasonal modulation, we compute the monthly climatology of submesoscale enstrophy based on the 2-yr data (Fig. 10). The results show an irregular annual cycle with a steep peak but a flat trough. Specifically, the peak of enstrophy occurs in March, and the second and third largest values occur in February and April, respectively; from May to December, the enstrophy keeps low and its magnitude has small monthly variations. It is worth noting that the peak of submesoscale enstrophy does not coincide with the MLD maximum, which occurs in January in our observation region (Fig. 10b). Instead, the top three large-enstrophy months (i.e., February–April) are actually during the sharply decreasing period of the MLD. Note that although the mean net surface heat flux is still negative in February (which tends to deepen the mixed layer), the mixed layer is shoaling possibly due to the restratification effect of the strong submesoscales (e.g., Mahadevan et al. 2012; Sasaki et al. 2014; du Plessis et al. 2017). This point is supported by the important role of submesoscale VHF in the mixed layer heat budget that will be discussed in detail in section 4b. By comparing the monthly enstrophy with the MSR, we find that in the strong-submesoscales period

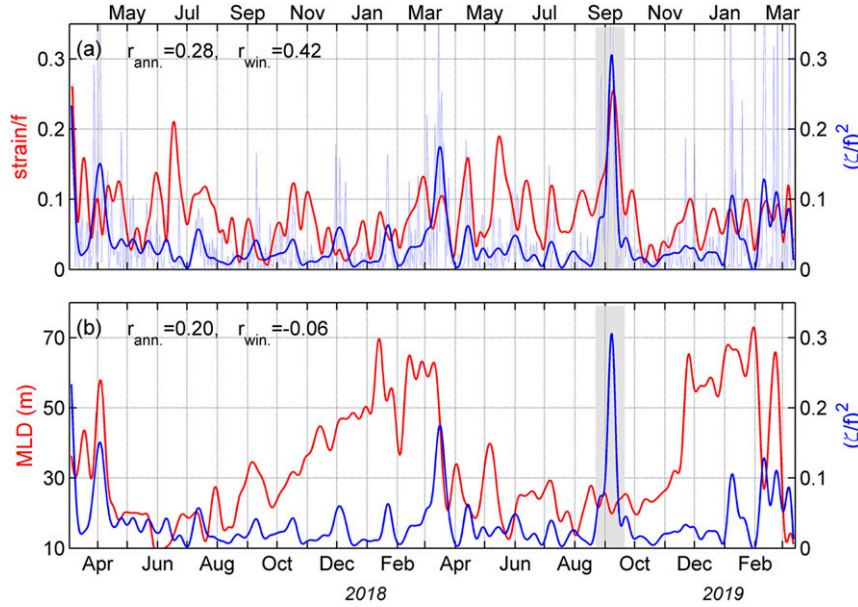


FIG. 9. (a) Comparison between the upper-layer averaged (between 50 and 100 m) mesoscale strain rate (red; normalized by dividing f) and submesoscale enstrophy (blue; normalized by dividing f^2). The blue thin and thick lines denote the original and 15-day low-pass-filtered results, respectively. The typhoon-related submesoscale event is marked by gray shading, which is excluded in the further analysis. Correlation coefficients between red and blue thick lines for the whole time series (except the gray-shading period, i.e., $r_{ann.}$) and for the winter–spring season (i.e., $r_{win.}$) are marked in the figure. The 95% significance levels for the $r_{ann.}$ and $r_{win.}$ are ± 0.20 and ± 0.31 , respectively (based on Monte Carlo simulations). (b) As in (a), but the red line denotes MLD.

between February and April, the MSR is also at a high level (Fig. 10a). Although the MSR remains strong between May and July, however, the submesoscale enstrophy is quite weak. The results presented above can be synthesized as follows. First, a relatively deep mixed layer is the prerequisite to energize submesoscales and the strong MSR in summer alone cannot generate the enhanced submesoscales. Second, in the winter–spring season with a relatively deep MLD, the mesoscale strain seems to play an important role in generating the submesoscales. Third, the submesoscales may be dynamically important in re-stratifying the mixed layer in the winter–spring season.

e. Energetics of submesoscales

If neglecting the horizontal advection and dissipation terms, baroclinic conservation (BC) and barotropic conversion (BT) are the primary source or sink in the submesoscale KE budget. To examine the energetics of the submesoscales, we calculate the BC and BT terms based on the first-year data (note that w is not available for the second year). Here, the BC and BT are defined as

$$BC = -\frac{g}{\rho_0} \overline{\rho' w'}, \quad (6)$$

$$BT = -\left(\overline{u'v'} \frac{\partial \bar{u}}{\partial y} + \overline{u'u'} \frac{\partial \bar{u}}{\partial x} + \overline{u'v'} \frac{\partial \bar{v}}{\partial x} + \overline{v'v'} \frac{\partial \bar{v}}{\partial y} \right), \quad (7)$$

where the primes denote submesoscale anomalies obtained by 15-day high-pass filter and the overbars denote 15-day running

means. Note that the terms associated with vertical shear (i.e., $-\overline{w' \partial \bar{u} / \partial z}$) have been neglected in Eq. (7) because they are found to be several times smaller than the horizontal shear terms (Fig. 11b). The upper-layer averaged BC (between 50

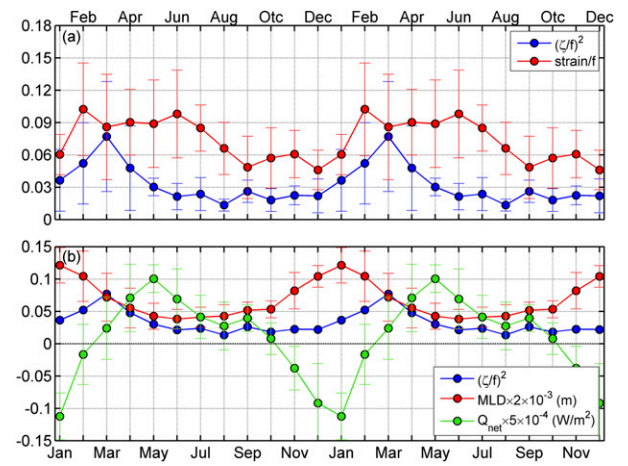


FIG. 10. (a) As in Fig. 9a, but for the climatologically monthly mean results obtained from the 2-yr-long moored data. Vertical bars are standard deviations associated with the circles. For a better visual effect, the annual cycle is repeated twice. (b) As in (a), but the red and green lines denote the MLD and ECMWF surface net heat flux, respectively.

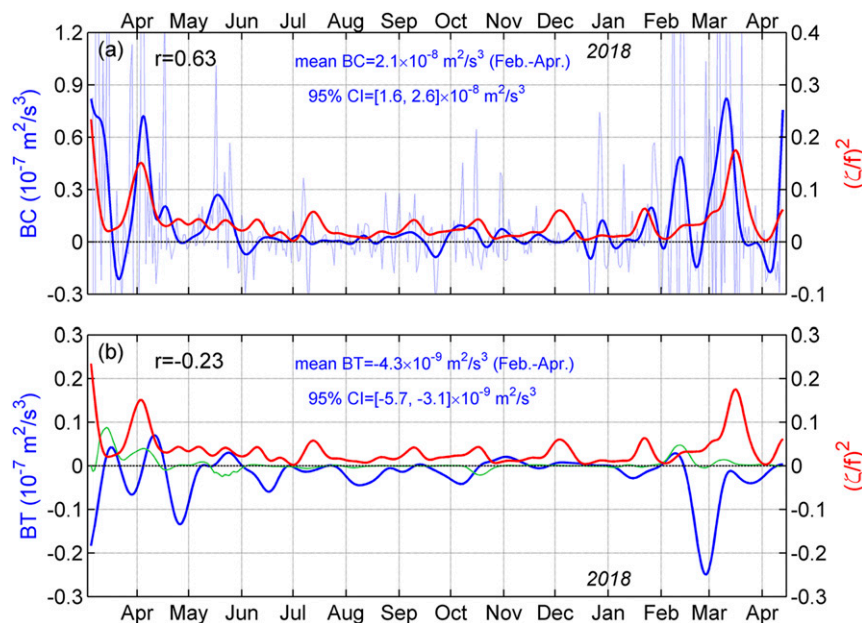


FIG. 11. (a) Time series of the upper-layer averaged (between 50 and 100 m) BC (blue) and normalized submesoscale enstrophy (red). The thick and thin lines denote results with and without 15-day running mean, respectively. The correlation coefficient between the red and blue thick lines is marked on the top-left corner. The mean BC between February and April and the associated 95% confidence intervals are also marked. (b) As in (a), but the blue line denotes the BT. The green line denotes the BT associated with vertical shear terms that have been neglected in Eq. (7).

and 100 m) shows that the BC is overall positive throughout the year and it is significantly enhanced between February and April, but is quite weak between June and December (Fig. 11a). The BC is highly correlated with the submesoscale enstrophy with their correlation coefficient reaching 0.63. This suggests that the BC term, or the vertical buoyancy flux, plays an important role in feeding the submesoscales. On the contrary, the BT is generally negative throughout the year and its negative values are elevated between February and April (Fig. 11b). The negative BT indicates that the submesoscales tend to transfer their KE inversely to the larger scales, i.e., mesoscale eddies. In other words, the KE exchange from the submesoscale and mesoscale interactions works as a sink for the submesoscale KE (i.e., an inverse KE cascade). During the strong-submesoscales period between February and April, the mean values of BC and BT are 2.1×10^{-8} and $-4.3 \times 10^{-9} \text{ m}^2 \text{ s}^{-3}$, respectively, with their respective 95% confidence levels of $[1.6, 2.6] \times 10^{-8}$ and $[-5.7, -3.1] \times 10^{-9} \text{ m}^2 \text{ s}^{-3}$ (computed using bootstrap method). Because the magnitude of BT is on average ~ 4 times smaller than the BC, the sum of BC and BT is still positive in the winter–spring season. To keep the balance, the net submesoscale KE gained from the BT + BC has to be dissipated or transferred to smaller scales through a forward cascade (Zhang et al. 2020). Note that given the spatial variabilities of BC and BT, we are not sure to what degree the present results can represent the whole STCC region. But, we think the time-mean results considered here (i.e., positive BC, negative BT, and positive BC + BT) are at least qualitatively true, which are generally consistent with recent simulation-based studies in a large spatial domain (e.g., Dong et al. 2020; Zhang et al. 2020).

Centrifugal (or inertial) instability and symmetric instability are thought as two important mechanisms for dissipation or forward cascade of the submesoscale energy (e.g., McWilliams 2016). Here, the potential roles of these two instabilities in the submesoscale energetics are evaluated based on the 2-yr moored data. The results in Figs. 4 and 5 suggest that except for the special submesoscale event in September of 2018, all Rossby numbers are larger than -1 . This indicates that the criterion for centrifugal instability that requires minus absolute vorticity in the north hemisphere, is not met and the centrifugal instability should not be regarded as the dissipation mechanism of the submesoscale KE here. With respect to the symmetric instability, its occurrence requires Ertel PV to be negative in the north hemisphere (Thomas et al. 2013; Bachman et al. 2017). Here, the Ertel PV is defined as

$$\text{EPV} = \left(-\frac{\partial v}{\partial z} + \frac{\partial w}{\partial y} \right) \frac{\partial b}{\partial x} + \left(\frac{\partial u}{\partial z} - \frac{\partial w}{\partial x} \right) \frac{\partial b}{\partial y} + (f + \zeta) \frac{\partial b}{\partial z}, \quad (8)$$

where $b = -g\rho/\rho_0$ is buoyancy. Given that the horizontal gradient of w is not available from the observations and that its magnitude is usually much smaller than the vertical shear of horizontal velocity, $\partial w/\partial x$ and $\partial w/\partial y$ in Eq. (8) are neglected in practice. For the second year, the horizontal buoyancy gradients are estimated using velocity shear by assuming the thermal wind balance. Figure 12 shows the depth–time plots of the Ertel PV calculated using the 2-yr moored data. Corresponding to the depth–time variations of the stratification, the Ertel PV is larger in summer and near the thermocline but smaller in winter and in the mixed layer. Negative Ertel PVs are indeed observed

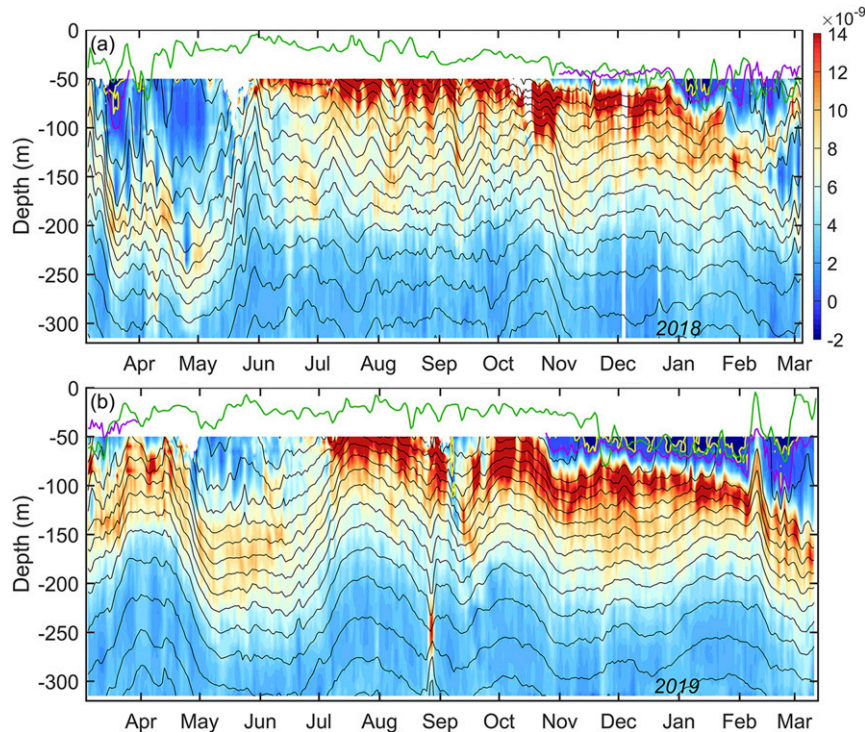


FIG. 12. As in Fig. 4, but for the Ertel PV (color shading). Black lines are contours of temperature same with those in Fig. 2c. The zero Ertel PV contour is marked by yellow lines.

but they are primarily confined within the mixed layer between December and April. During this period, the percentage of negative Ertel PVs reaches 28% at the 50-m depth (it is 40% if only the period of December–February is considered) but it sharply decreases to 3% at 70m. Note that for all of these negative Ertel PVs, the vorticity term $(f + \zeta)\partial b/\partial z$ is always positive, which therefore excludes the occurrence of centrifugal instability. The negative Ertel PVs here are actually caused by the combination of weakly (gravitational) stable stratification and strong vertical shear of currents. Given the vertical decrease of negative Ertel PVs' percentage, it may be even higher above 50 m that is beyond our observational range. The above result indicates that the symmetric instability may frequently occur in the mixed layer in the winter–spring season and could be a potential mechanism that dissipates the submesoscale KE. Theoretically, turbulence associated with symmetric instability grows by extracting energy from the geostrophic shear of submesoscales. However, the exact role of symmetric instability in the submesoscale KE budget cannot be quantified here because its time and length scales [from minutes to 1 h and 50–2500 m according to Bachman et al. (2017)] are too small to be resolved by our available observations.

4. Discussion

a. Generation mechanisms of submesoscales

The positive BC and negative BT in Fig. 11 suggest the baroclinic nature of the submesoscale generation processes and that the barotropic instability is an unlikely generation mechanism for the submesoscales here, although it is found to

be important for the submesoscale generations in topographic wakes or near-coast regions (e.g., Srinivasan et al. 2019; Tedesco et al. 2019; Zhang et al. 2020). Theoretically, the MLI, strain-induced frontogenesis, and turbulent thermal wind-induced frontogenesis can all generate positive BC with a corresponding restratifying effect in the mixed layer (McWilliams 2016). For the BC caused by the turbulent thermal wind, it scales with the eddy viscosity associated with wind-driven turbulence, which is strongly suppressed beneath the mixed layer (e.g., Gula et al. 2014). Given that the submesoscales observed in our study (enstrophy or KE_a) can penetrate far beneath the mixed layer, the convergent velocity-induced frontogenesis associated with turbulent thermal wind mentioned in Barkan et al. (2019) should not be a dominant generation mechanism here. With respect to the BCs caused by MLI and strain-induced surface frontogenesis, they scale with $(H_b^2/f)|\nabla b|^2$ and $\alpha(H_b^2/f^2)|\nabla b|^2$, respectively, where H_b is the MLD and α is the MSR (Fox-Kemper et al. 2008; McWilliams 2016). Given that the magnitude of horizontal buoyancy gradient $|\nabla b|$ can be strengthened by strain-induced frontogenesis, the BC of MLI is also associated with the MSR, albeit in an indirect way. This means that the strength of submesoscales generated either by MLI or by strain-induced frontogenesis would be closely related to both the MLD and MSR.

Based on the observed quantities in Figs. 9–11 alone, it is difficult to determine which mechanism is more important. However, we argue that in the final generation stage of submesoscales, the MLI should play a more dominant role for the following two reasons. First, the power spectrum of the upper-layer BC shows energy peaks at 6–9 days, which agree with the

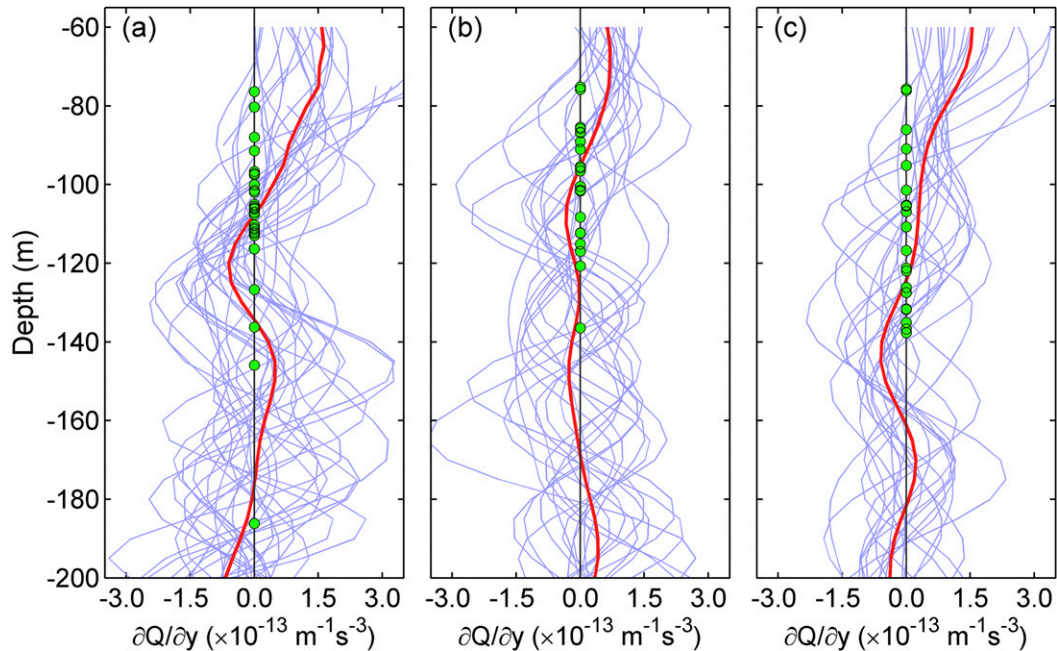


FIG. 13. Vertical profiles of the meridional gradient of the background PV during three strong-submesoscales periods: (a) 6 Mar–3 Apr 2017, (b) 3–23 Mar 2018, and (c) 6–26 Feb 2019. Blue lines and red line denote the daily results and the composite mean result, respectively. The first cross-zero position for each profile is marked using green dot. Note that in order to make the composite meaningful, the daily profile is multiplied by -1 if its upper most value is negative.

growth time scale (i.e., 7–8 days) of the most unstable wave in the MLI analysis based on parameters in the STCC region (Qiu et al. 2014). Second, the submesoscales generated by mesoscale strain-induced surface frontogenesis are strongly surface trapped and are unable to penetrate far beneath the mixed layer (Lapeyre and Klein 2006; Callies et al. 2016), which is different from what is observed. For the MLI, on the other hand, it can energize the whole upper mixed or weakly stratified layer through the interactions between the surface and bottom edge waves (e.g., Callies et al. 2016). Recently, several studies in the ACC and OSMOSIS regions have pointed out that deep-reaching mesoscale strain can also result in frontogenesis in ocean interior far beneath the mixed layer (Yu et al. 2019; Siegelman et al. 2020; Siegelman 2020). However, it may not explain the submesoscale generations in the STCC region because energetic submesoscales are nearly absent in summer when MSR is strongest.

Theoretically, the necessary condition for baroclinic instability requires that the horizontal gradient of background PV ($Q = fN^2$) changes sign in the vertical direction (Vallis 2006). By adopting the thermal wind assumption, the meridional gradient of the background PV is estimated using $Q = \beta N^2 - f^2 \partial^2 \bar{u} / \partial z^2$, where the overbar denotes mesoscale mean (i.e., 15-day running mean). In Fig. 13, we show the vertical distribution of Q_y during the three strong-submesoscales periods over the 2 years. It is found that the first cross-zero point is not within the mixed layer but occurs between 90 and 130 m, which coincides with the weakly stratified transitional layer between the mixed layer and the thermocline (recall Fig. 12). In other words, the bottom edge waves during the baroclinic instability occur within this transitional layer rather than at the base of the traditionally defined mixed layer. Given this, the

baroclinic instability feeding the submesoscales here is more properly called mixed transitional layer instability rather than MLI (J. Callies 2020, personal communication). The sign change of Q_y in Fig. 13 may explain why the observed submesoscales extend far beneath the mixed layer. Although the above analysis provides further evidence of the baroclinic instability mechanism for the submesoscale generations, it does not mean that the strain-induced frontogenesis is unimportant. Actually, it plays an important role in strengthening the preexisting fronts and provides a favorable condition (by increasing the available potential energy) for the development of baroclinic instability (Zhang et al. 2020). That is why the strength of submesoscales is enhanced during the strong-MSR periods in the winter–spring season.

b. Impact of submesoscales on mixed layer heat budget

The positive submesoscale BC means an upward VHF that warms the upper ocean. Here, the role of submesoscales in the upper-ocean heat budget is quantified by comparing the equivalent VHF with the concurrent net surface heat flux from the ECMWF ERA-Interim reanalysis product (Dee et al. 2011). The VHF is computed using $C_p \rho_0 T' w'$, where $C_p = 4000 \text{ J kg}^{-1} \text{ } ^\circ\text{C}^{-1}$ is specific heat capacity (Su et al. 2018). The result in Fig. 14 shows that the submesoscale VHF averaged between 50 and 100 m is much weaker than the surface heat flux in most of the months, but their magnitudes are comparable in February and March when the surface heat flux shifts from negative to positive. In March (February), the monthly mean submesoscale VHF reaches 40.4 W m^{-2} (19.0 W m^{-2}) and accounts for 85% (-57%) of the surface heat flux. This result demonstrates that in the late winter and early spring (i.e., the

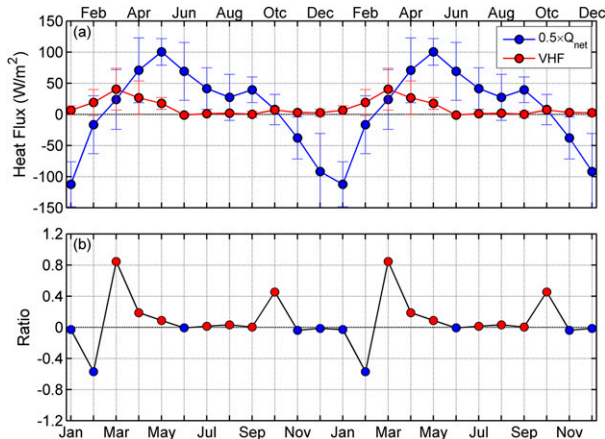


FIG. 14. (a) As in Fig. 10a, the red and blue lines denote the submesoscale VHF and surface net heat flux (multiplied by 0.5), respectively. (b) Ratio between the monthly mean submesoscale VHF and surface net heat flux. The positive and negative values are indicated using red and blue dots, respectively.

transitional period from surface cooling to warming), the submesoscale VHF could play a leading-order role in the upper-ocean heat budget and contributes to the rapid shoaling of mixed layer during this period (Figs. 9b and 10b; Mahadevan et al. 2012; du Plessis et al. 2017). It should be pointed out that the above estimated VHF is only associated with the subinertial submesoscales, and the total submesoscale VHF may be even larger when the superinertial component is considered (Su et al. 2020).

c. Seasonality of submesoscales

The submesoscales observed here are stronger in the winter–spring season but weaker in the summer–autumn season, which are generally consistent with the results from submesoscale-permitting numerical simulations (e.g., Mensa et al. 2013; Sasaki et al. 2014; Qiu et al. 2018; Su et al. 2018). However, it should be pointed out that when discussing the seasonality of submesoscales, we do not include the SCVs and the strong submesoscale event associated with the typhoons. The two lens-like SCVs occurred in the winter–spring season but the prism-like SCV and the typhoon-related submesoscale event occurred in the summer–autumn season. For the lens-like SCVs, their generations are most possibly associated with frontogenesis-induced subduction processes as pointed out by a previous simulation (Spall 1995) and recent observations (Zhang et al. 2015b; Li et al. 2017). With respect to the prism-like SCV and typhoon-related submesoscale current, however, their generation dynamics are unclear at present and will be left for future studies. In addition, we should also note that because the mixed layer is very shallow (10–20 m) and the corresponding deformation radius is much smaller (smaller than 1 km) in summer, the configuration of our SM mooring array may have prevented us from capturing the submesoscales at that time. Actually, how to observe the mixed layer submesoscales in summer still is a technical challenge for the community. Therefore, whether the submesoscales in summer are indeed weak as found by the present-resolution

observations and numerical simulations is still an open question (J.C. McWilliams 2019, personal communication).

5. Conclusions

In the present study, 2-yr-long data collected from one mesoscale and one submesoscale mooring arrays between March 2017 and March 2019 (i.e., the SubMESI experiment) are used to investigate the submesoscales in the upper ocean of the northwestern Pacific STCC region. The submesoscale properties such as Ro (relative vorticity), w , and Ertel PV are calculated based on the moored data, giving the basics to examine the dynamical features and mechanisms of the submesoscales. To the authors' best knowledge, the SubMESI mooring arrays provided the first long-term continuous submesoscale observations in the subtropical gyre featured by moderate levels of both EKE and MLD. The main conclusions of this study are summarized as follows:

- (i) Strong submesoscale motions with order one Ro and large w (with magnitude of $10\text{--}50\text{ m day}^{-1}$) are directly observed in the STCC upper ocean. In contrast to the mesoscale eddies, the submesoscales have a much shorter time scale with the Eulerian period shorter than 15 days. Although the intensity of the submesoscales generally decreases with depth, their signals are not confined within the mixed layer but can penetrate far beneath, and sometimes reach deeper than, 150 m.
- (ii) The upper-ocean submesoscales display a clear seasonality, whose strengths are stronger in the winter–spring season (i.e., February–April) but weaker in the summer–autumn season. The strongest submesoscales occur in March, lagging two months behind the maximum MLD in January. In the winter–spring season, the submesoscales also show significant intraseasonal variations and are well correlated with the mesoscale strain rate associated with the propagating mesoscale eddies.
- (iii) Accompanied by the large Ro and w , the submesoscales show strong ageostrophic KE and account for 35% of the total submesoscale KE in the winter–spring season in the upper 50–100-m layer. This result cautions that care is needed in treating the submesoscales as quasigeostrophic motions or diagnosing their horizontal velocity from satellite sea surface height data based on geostrophy.
- (iv) Energetics analysis suggests that the submesoscales gain their KE from the BC term but tend to transfer their KE inversely to mesoscale eddies through the BT term. The positive BC results in an equivalent upward heat flux as large as 40.4 W m^{-2} (19.0 W m^{-2}) in March (February), comparable in magnitude with the net surface heat fluxes (47.7 and -33.3 W m^{-2} in March and February, respectively). This suggests that in the later winter and early spring when the atmospheric forcing shifts from cooling to warming, the submesoscales can be of fundamental importance for the upper-ocean heat budget.
- (v) The sum of the BC and BT terms is positive in the winter–spring season, demonstrating that dissipation or direct cascade must play a role in order to keep the balance of the submesoscale KE budget. The Ertel PV field shows a considerable portion of negative values within the mixed layer in this season and symmetric instability may be a

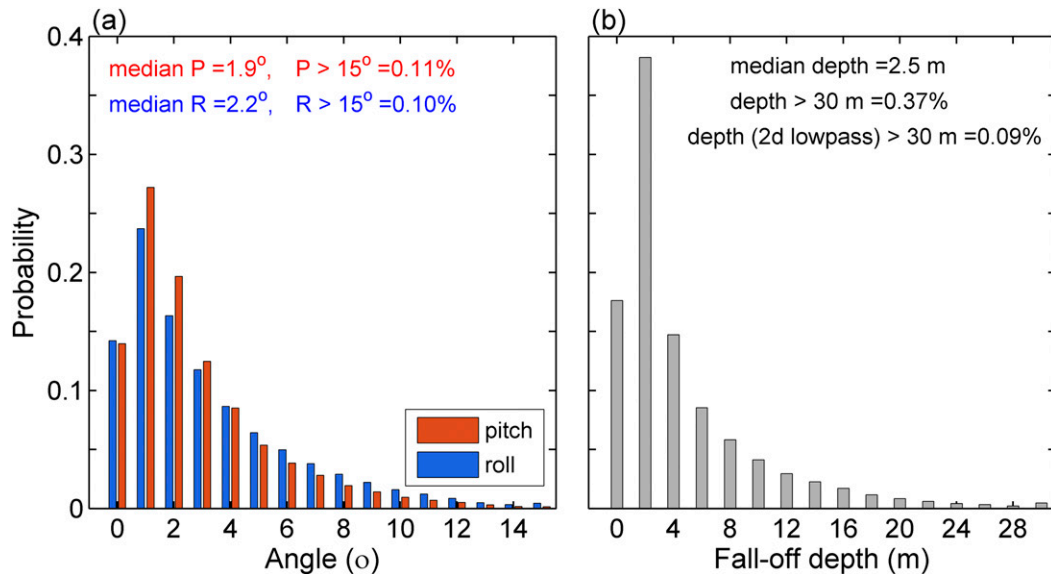


FIG. A1. (a) Probability density distribution of the absolute values of hourly pitch (red) and roll (blue) measured by all ADCPs on the SM moorings during the 2-yr period. (b) As in (a), but for the hourly fall-off depths of the ADCPs. The median values of pitch, roll, and fall-off depth as well as the percentages of pitch $> 15^\circ$, pitch $> 15^\circ$, and fall-off depth > 30 m are shown in the figures.

candidate mechanism responsible for the direct cascade of submesoscale KE.

- (vi) The submesoscales observed here are likely generated by a combination of baroclinic instability in the mixed and transitional layers and strain-induced frontogenesis. However, in the final generation stage of submesoscales, we think the baroclinic instability is likely to play a more important role based on the energy peak in the BC spectrum as well as the relatively deep penetration of the observed submesoscales.

In addition to the above results, the observations also captured two anticyclonic and one cyclonic SCVs as well as a peculiar typhoon-related submesoscale event at different seasons and depths. These events suggest the diversity of submesoscales in the real ocean and they need to be investigated in detail in future studies. Although the observations are collected in the north-western subtropical Pacific, the main features and mechanisms of submesoscales found here should also be qualitatively true for the other STCC regions because they share similar dynamical background, such as elevated EKE and moderate MLD. Finally, it should be noted that the submesoscales discussed in this study are only associated with the subinertial currents that can be resolved by the SM subsurface mooring array. To understand the near-surface submesoscales above ~ 50 m, or those associated with superinertial and even smaller-scale currents, specially designed and even higher-resolution observations are needed in the future.

Acknowledgments. This work was jointly supported by the National Natural Science Foundation of China (Grants 41706005, 91958205, and 91858203), the National Key Research and Development Program of China (Grants 2016YFC1402605, 2018YFA0605702), the Global Change and Air-Sea Interaction Project (GASI-IPOVAI-01-03), and the Fundamental Research

Funds for the Central Universities (Grants 202041009, 201861006, 202013028). The altimeter data, HYCOM reanalysis data, and surface heat flux data used in this study are downloaded from the CMEMS website (<http://marine.copernicus.eu/>), the HYCOM website (<http://www.hycom.org/>), and the ECMWF website (<http://apps.ecmwf.int/>), respectively. Ones who want to get access to the moored data analyzed here should contact the corresponding author. Several temperature sensors used here were developed by Deep-sea Sensor Group operated by Dr. Chuan Tian from Institute of Deep-sea Science and Engineering, Chinese Academy of Sciences. The authors appreciate their assistance. The helpful discussions with James McWilliams, Andrew Thompson, and Jörn Callies are appreciated. The authors thank two anonymous reviewers for their helpful comments. Author contributions of this paper are as follows: Z.Z. proposed the idea, designed the SubMESI experiment, and wrote the manuscript. J.T. led the research, organized the cruises, and performed the SubMESI experiment. X.Z. analyzed the data under Z.Z.'s instruction. B.Q. contributed to the manuscript writing and results interpretation. W.Z., C.Z., and X.H. contributed to improving the manuscript.

APPENDIX A

Assessment of Velocity and Vorticity Errors Caused by Swing of Mooring

One kind of ADCP velocity error is associated with the tilt of ADCP. In Fig. A1a, we show the PDFs of the absolute values of pitch and roll measured by all the ADCPs on the SM moorings. Given the special design of the SM moorings (e.g., shallower water depths and more buoyancy for the main floating body), swing of the mooring and, thus, tilt of the ADCPs are quite weak. During the 2-yr period, the median angle of pitch and roll are 1.9° and

2.2°, respectively. The percentage of pitch and roll angles exceeding 15° (i.e., the maximum measurement range of the tilt sensor) are only 0.11% and 0.10%, respectively, which are less than one day for time length. The ADCP velocity errors caused by ADCP tilt is proportional to the square of the sine of the pitch and roll errors (RD Instruments 2011). Considering that within the measurement range (i.e., smaller than 15°), the tilt sensor on ADCPs has an accuracy of 0.5° (RD Instruments 2007), the velocity error of 1 m s^{-1} caused by the tilt should be only $7.6 \times 10^{-5} \text{ m s}^{-1}$ [i.e., $1 \text{ m s}^{-1} \times \sin^2(0.5^\circ)$]. This velocity error is three orders of magnitude smaller than the typical submesoscale velocities with $O(0.1) \text{ m s}^{-1}$ and can therefore be neglected.

Another kind of ADCP velocity errors is caused by the horizontal swing of the ADCP itself due to strong currents. Figure A1b shows the PDF of the fall-off depths (FDs) of the ADCPs calculated using the difference between the instantaneous ADCP pressures and the minimum ADCP pressure (i.e., the mooring is vertical without swing). Corresponding to the small tilt of ADCPs, the FDs are also generally small. The median FD and the percentage of $\text{FD} > 30 \text{ m}$ are only 2.5 m and 0.37%, respectively. Note that the horizontal swing (or vertical excursion) of the mooring is primarily caused by the semidiurnal and diurnal tidal currents. If a 2-day low-pass filter is applied to the FDs to focus on the subinertial component, the percentage of $\text{FD} > 30 \text{ m}$ becomes only 0.09%, which is equivalent to 0.66 days in time length. In the region of 1000 m water depth, the vertical excursion of 30 m for an ADCP at 400 m beneath surface will result in a horizontal swing distance of 187 m according to the Pythagorean theorem (i.e., $\sqrt{600^2 - 570^2} \text{ m}$). If this horizontal swing is caused by submesoscale (mesoscale) current with a mean half period of 3 days (30 days), the corresponding horizontal velocity will be $7.2 \times 10^{-4} \text{ m s}^{-1}$ ($7.2 \times 10^{-5} \text{ m s}^{-1}$), which is two (three) orders of magnitude smaller than the submesoscale (mesoscale) velocities. Therefore, even for the worst occasion, the velocity errors caused by the horizontal swing of ADCPs can still be neglected compared with the mesoscale and submesoscale signals focused on here.

The horizontal swing of moorings will also result in calculation errors for the horizontal gradient of velocity (also temperature) because it may cause uncertainty of the distance between two moorings. Here, we assess the largest possible error for ζ due to the above issue by considering the worst scenario that the distance between two SM moorings has an error of 187 m (in the real situation, the error is much smaller than this because when the horizontal scale of currents is larger than the mooring distance, the moorings tend to swing together). When we use the central differential to calculate ζ , the 187-m error for the original distance of 4000 m will result in a relative error of 6%. This means that during the whole observation period, the error for ζ (and also the other horizontal gradients) due to the uncertainty of mooring positions should by no means exceed 6%.

APPENDIX B

Calculation of Strain Rate Based on Three Observational Points of a Triangle

The strain rate in the Cartesian coordinates is defined in Eq. (5) of the main text. Given that the three moorings used to

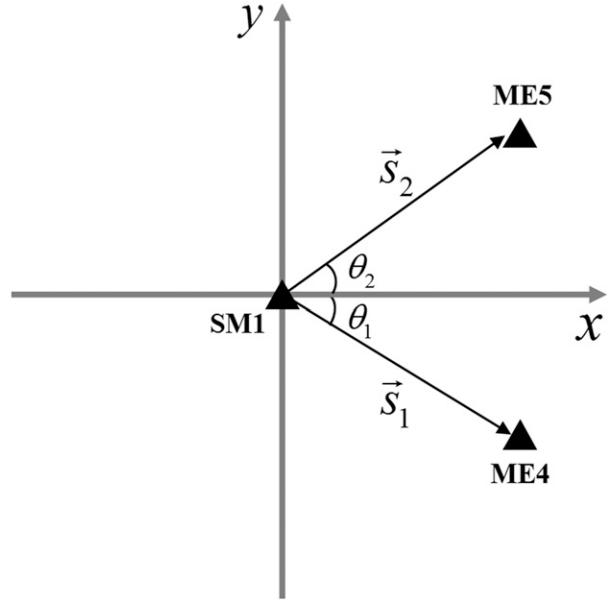


FIG. B1. Locations of the moorings SM1, ME4, and ME5 (black triangles) in Cartesian coordinates. The mooring SM1 is set at the origin of coordinates. The direction vectors from SM1 to ME4 and ME5 are denoted using \mathbf{S}_1 and \mathbf{S}_2 , respectively. The θ_1 and θ_2 are direction angles of these two vectors relative to the positive x coordinate (i.e., their values are negative and positive, respectively).

calculate the strain rate do not make a right triangle with the legs along the x or y coordinate, we in the following deduce the calculation formula using the three points of a triangle. Without loss of generality, we take the triangle composed of moorings SM1, ME4, and ME5 as an example to show this. The direction vectors and angles used here are shown in Fig. B1. For any scalar A , its directional derivative along \mathbf{S} can be expressed as a function of its gradient and the directional angle \mathbf{S} , i.e., $\partial A / \partial s = \partial A / \partial x \cos \theta + \partial A / \partial y \sin \theta$. In this case, the directional derivatives of the zonal velocity u along \mathbf{S}_1 and \mathbf{S}_2 in Fig. B1 can be calculated using

$$\begin{cases} \frac{\partial u}{\partial s_1} = \frac{\partial u}{\partial x} \cos \theta_1 + \frac{\partial u}{\partial y} \sin \theta_1 \\ \frac{\partial u}{\partial s_2} = \frac{\partial u}{\partial x} \cos \theta_2 + \frac{\partial u}{\partial y} \sin \theta_2 \end{cases}, \quad (\text{B1})$$

where meanings of the parameters are demonstrated in Fig. B1. Through solving these linear algebraic equations, we get the gradient of u in the Cartesian coordinates

$$\begin{cases} \frac{\partial u}{\partial x} = \frac{1}{\sin(\theta_2 - \theta_1)} \left(\frac{\partial u}{\partial s_1} \sin \theta_2 - \frac{\partial u}{\partial s_2} \sin \theta_1 \right) \\ \frac{\partial u}{\partial y} = \frac{1}{\sin(\theta_2 - \theta_1)} \left(-\frac{\partial u}{\partial s_1} \cos \theta_2 + \frac{\partial u}{\partial s_2} \cos \theta_1 \right) \end{cases}. \quad (\text{B2})$$

The directional derivatives of u and the angles θ_1 and θ_2 can be easily obtained from the three moorings. The gradient of the meridional velocity v can be obtained in the similar way. By substituting the gradients of u and v into Eq. (5), the strain rate can be finally calculated.

REFERENCES

- Adams, K. A., P. Hosegood, J. R. Taylor, J.-B. Sallée, S. Bachman, R. Torres, and M. Stamper, 2017: Frontal circulation and submesoscale variability during the formation of a Southern Ocean mesoscale eddy. *J. Phys. Oceanogr.*, **47**, 1737–1753, <https://doi.org/10.1175/JPO-D-16-0266.1>.
- Bachman, S. D., B. Fox-Kemper, J. Taylor, and L. Thomas, 2017: Parameterization of frontal symmetric instabilities. I: Theory for resolved fronts. *Ocean Modell.*, **109**, 72–95, <https://doi.org/10.1016/j.ocemod.2016.12.003>.
- Barkan, R., K. B. Winters, and S. G. L. Smith, 2015: Energy cascades and loss of balance in a reentrant channel forced by wind stress and buoyancy fluxes. *J. Phys. Oceanogr.*, **45**, 272–293, <https://doi.org/10.1175/JPO-D-14-0068.1>.
- , J. C. McWilliams, A. F. Shchepetkin, M. J. Molemaker, L. Renault, A. Bracco, and J. Choi, 2017: Submesoscale dynamics in the northern Gulf of Mexico. Part I: Regional and seasonal characterization, and the role of river outflow. *J. Phys. Oceanogr.*, **47**, 2325–2346, <https://doi.org/10.1175/JPO-D-17-0035.1>.
- , M. J. Molemaker, K. Srinivasan, J. C. McWilliams, and E. A. Dasaro, 2019: The role of horizontal divergence in submesoscale frontogenesis. *J. Phys. Oceanogr.*, **49**, 1593–1618, <https://doi.org/10.1175/JPO-D-18-0162.1>.
- Boccaletti, G., R. Ferrari, and B. Fox-Kemper, 2007: Mixed layer instabilities and restratification. *J. Phys. Oceanogr.*, **37**, 2228–2250, <https://doi.org/10.1175/JPO3101.1>.
- Brannigan, L., 2016: Intense submesoscale upwelling in anticyclonic eddies. *Geophys. Res. Lett.*, **43**, 3360–3369, <https://doi.org/10.1002/2016GL067926>.
- Buckingham, C. E., and Coauthors, 2016: Seasonality of submesoscale flows in the ocean surface boundary layer. *Geophys. Res. Lett.*, **43**, 2118–2126, <https://doi.org/10.1002/2016GL068009>.
- Callies, J., R. Ferrari, J. M. Klymak, and J. Gula, 2015: Seasonality in submesoscale turbulence. *Nat. Commun.*, **6**, 6862, <https://doi.org/10.1038/ncomms7862>.
- , G. Flierl, R. Ferrari, and B. Fox-Kemper, 2016: The role of mixed-layer instabilities in submesoscale turbulence. *J. Fluid Mech.*, **788**, 5–41, <https://doi.org/10.1017/jfm.2015.700>.
- Cao, H., Z. Jing, B. Fox-Kemper, T. Yan, and Y. Qi, 2019: Scale transition from geostrophic motions to internal waves in the northern South China Sea. *J. Geophys. Res. Oceans*, **124**, 9364–9383, <https://doi.org/10.1029/2019JC015575>.
- Capet, X., J. C. McWilliams, M. J. Molemaker, and A. F. Shchepetkin, 2008a: Mesoscale to submesoscale transition in the California current system. Part II: Frontal processes. *J. Phys. Oceanogr.*, **38**, 44–64, <https://doi.org/10.1175/2007JPO3672.1>.
- , —, —, and —, 2008b: Mesoscale to submesoscale transition in the California Current System. Part III: Energy balance and flux. *J. Phys. Oceanogr.*, **38**, 2256–2269, <https://doi.org/10.1175/2008JPO3810.1>.
- Chelton, D. B., R. A. de Szoeke, M. G. Schlax, K. E. Naggar, and N. Siwertz, 1998: Geographical variability of the first baroclinic Rossby radius of deformation. *J. Phys. Oceanogr.*, **28**, 433–460, [https://doi.org/10.1175/1520-0485\(1998\)028<0433:GVOTFB>2.0.CO;2](https://doi.org/10.1175/1520-0485(1998)028<0433:GVOTFB>2.0.CO;2).
- , M. G. Schlax, and R. M. Samelson, 2011: Global observations of nonlinear mesoscale eddies. *Prog. Oceanogr.*, **91**, 167–216, <https://doi.org/10.1016/j.pocean.2011.01.002>.
- D’Asaro, E., C. Lee, L. Rainville, R. Harcourt, and L. Thomas, 2011: Enhanced turbulence and energy dissipation at ocean fronts. *Science*, **332**, 318–322, <https://doi.org/10.1126/science.1201515>.
- , and Coauthors, 2018: Ocean convergence and the dispersion of flotsam. *Proc. Natl. Acad. Sci. USA*, **115**, 1162–1167, <https://doi.org/10.1073/pnas.1718453115>.
- de Boyer Montégut, C., G. Madec, A. S. Fischer, A. Lazar, and D. Iudicone, 2004: Mixed layer depth over the global ocean: An examination of profile data and a profile-based climatology. *J. Geophys. Res.*, **109**, C12003, <https://doi.org/10.1029/2004JC002378>.
- Dee, D. P., and Coauthors, 2011: The ERA-Interim reanalysis: Configuration and performance of the data assimilation system. *Quart. J. Roy. Meteor. Soc.*, **137**, 553–597, <https://doi.org/10.1002/qj.828>.
- Dong, J., B. Fox-Kemper, H. Zhang, and C. Dong, 2020: The seasonality of submesoscale energy production, content, and cascade. *Geophys. Res. Lett.*, **47**, e2020GL087388, <https://doi.org/10.1029/2020GL087388>.
- du Plessis, M., S. Swart, I. J. Anson, and A. Mahadevan, 2017: Submesoscale processes promote seasonal restratification in the Subantarctic Ocean. *J. Geophys. Res. Oceans*, **122**, 2960–2975, <https://doi.org/10.1002/2016JC012494>.
- Erickson, Z. K., A. F. Thompson, J. Callies, X. Yu, A. N. Garabato, and P. Klein, 2020: The vertical structure of open-ocean submesoscale variability during a full seasonal cycle. *J. Phys. Oceanogr.*, **50**, 145–160, <https://doi.org/10.1175/JPO-D-19-0030.1>.
- Flament, P., L. Armi, and L. Washburn, 1985: The evolving structure of an upwelling filament. *J. Geophys. Res.*, **90**, 11 765–11 778, <https://doi.org/10.1029/JC090iC06p11765>.
- Fox-Kemper, B., R. Ferrari, and R. Hallberg, 2008: Parameterization of mixed layer eddies. Part I: Theory and diagnosis. *J. Phys. Oceanogr.*, **38**, 1145–1165, <https://doi.org/10.1175/2007JPO3792.1>.
- , G. Danabasoglu, R. Ferrari, R. W. Hallberg, M. M. Holland, M. E. Maltrud, S. Peacock, and B. L. Samuels, 2011: Parameterization of mixed layer eddies. III: Implementation and impact in global ocean climate simulations. *Ocean Modell.*, **39**, 61–78, <https://doi.org/10.1016/j.ocemod.2010.09.002>.
- , and Coauthors, 2019: Challenges and prospects in ocean circulation models. *Front. Mar. Sci.*, **6**, 65, <https://doi.org/10.3389/fmars.2019.00065>.
- Fu, L.-L., D. B. Chelton, P.-Y. Le Traon, and R. Morrow, 2010: Eddy dynamics from satellite altimetry. *Oceanography*, **23**, 14–25, <https://doi.org/10.5670/oceanog.2010.02>.
- Gula, J., M. J. Molemaker, and J. C. McWilliams, 2014: Submesoscale cold filaments in the Gulf Stream. *J. Phys. Oceanogr.*, **44**, 2617–2643, <https://doi.org/10.1175/JPO-D-14-0029.1>.
- , —, and —, 2016a: Topographic generation of submesoscale centrifugal instability and energy dissipation. *Nat. Commun.*, **7**, 12811, <https://doi.org/10.1038/ncomms12811>.
- , —, and —, 2016b: Submesoscale dynamics of a Gulf Stream frontal eddy in the South Atlantic Bight. *J. Phys. Oceanogr.*, **46**, 305–325, <https://doi.org/10.1175/JPO-D-14-0258.1>.
- Holte, J., L. D. Talley, J. Gilson, and D. Roemmich, 2017: An Argo mixed layer climatology and database. *Geophys. Res. Lett.*, **44**, 5618–5626, <https://doi.org/10.1002/2017GL073426>.
- Hu, J. Y., J. P. Gan, Z. Y. Sun, J. Zhu, and M. H. Dai, 2011: Observed three-dimensional structure of a cold eddy in the southwestern South China Sea. *J. Geophys. Res.*, **116**, C05016, <https://doi.org/10.1029/2010JC006810>.
- Huang, J., and F. Xu, 2018: Observational evidence of subsurface chlorophyll response to mesoscale eddies in the North Pacific. *Geophys. Res. Lett.*, **45**, 8462–8470, <https://doi.org/10.1029/2018GL078408>.
- Jia, F., L. Wu, and B. Qiu, 2011: Seasonal modulation of eddy kinetic energy and its formation mechanism in the southeast

- Indian Ocean. *J. Phys. Oceanogr.*, **41**, 657–665, <https://doi.org/10.1175/2010JPO4436.1>.
- Klymak, J. M., and Coauthors, 2016: Submesoscale streamers exchange water on the north wall of the Gulf Stream. *Geophys. Res. Lett.*, **43**, 1226–1233, <https://doi.org/10.1002/2015GL067152>.
- Lapeyre, G., and P. Klein, 2006: Dynamics of the upper oceanic layers in terms of surface quasigeostrophy theory. *J. Phys. Oceanogr.*, **36**, 165–176, <https://doi.org/10.1175/JPO2840.1>.
- , —, and B. L. Hua, 2006: Oceanic restratification forced by surface frontogenesis. *J. Phys. Oceanogr.*, **36**, 1577–1590, <https://doi.org/10.1175/JPO2923.1>.
- Lévy, M., P. J. S. Franks, and K. S. Smith, 2018: The role of submesoscale currents in structuring marine ecosystems. *Nat. Commun.*, **9**, 4758, <https://doi.org/10.1038/s41467-018-07059-3>.
- Li, C., Z. Zhang, W. Zhao, and J. Tian, 2017: A statistical study on the subthermocline submesoscale eddies in the northwestern Pacific Ocean based on Argo data. *J. Geophys. Res. Oceans*, **122**, 3586–3598, <https://doi.org/10.1002/2016JC012561>.
- Lien, R.-C., B. Ma, Y. H. Cheng, C. R. Ho, B. Qiu, C. M. Lee, and M.-H. Chang, 2014: Modulation of Kuroshio transport by mesoscale eddies at the Luzon Strait entrance. *J. Geophys. Res. Oceans*, **119**, 2129–2142, <https://doi.org/10.1002/2013JC009548>.
- Mahadevan, A., 2016: The impact of submesoscale physics on primary productivity of plankton. *Annu. Rev. Mar. Sci.*, **8**, 161–184, <https://doi.org/10.1146/annurev-marine-010814-015912>.
- , and A. Tandon, 2006: An analysis of mechanisms for submesoscale vertical motion at ocean fronts. *Ocean Modell.*, **14**, 241–256, <https://doi.org/10.1016/j.ocemod.2006.05.006>.
- , E. D’Asaro, C. Lee, and M. J. Perry, 2012: Eddy-driven stratification initiates North Atlantic spring phytoplankton blooms. *Science*, **337**, 54–58, <https://doi.org/10.1126/science.1218740>.
- McGillicuddy, D. J., 2016: Mechanisms of physical-biological-biogeochemical interaction at the oceanic mesoscale. *Annu. Rev. Mar. Sci.*, **8**, 125–159, <https://doi.org/10.1146/annurev-marine-010814-015606>.
- , and Coauthors, 2007: Eddy/wind interactions stimulate extraordinary mid-ocean plankton blooms. *Science*, **316**, 1021–1026, <https://doi.org/10.1126/science.1136256>.
- McWilliams, J. C., 1985: Submesoscale, coherent vortices in the ocean. *Rev. Geophys.*, **23**, 165–182, <https://doi.org/10.1029/RG023i002p00165>.
- , 2016: Submesoscale currents in the ocean. *Proc. Roy. Soc. London*, **A472**, 20160117, <https://doi.org/10.1098/rspa.2016.0117>.
- , 2019: A survey of submesoscale currents. *Geosci. Lett.*, **6**, 3, <https://doi.org/10.1186/s40562-019-0133-3>.
- Mensa, J. A., Z. Garraffo, A. Griffo, T. M. Özgökmen, A. Haza, and M. Veneziani, 2013: Seasonality of the submesoscale dynamics in the Gulf stream. *Ocean Dyn.*, **63**, 923–941, <https://doi.org/10.1007/s10236-013-0633-1>.
- Molemaker, M. J., J. C. McWilliams, and W. K. Dewar, 2015: Submesoscale instability and generation of mesoscale anticyclones near a separation of the California Undercurrent. *J. Phys. Oceanogr.*, **45**, 613–629, <https://doi.org/10.1175/JPO-D-13-0225.1>.
- Naveira Garabato, A. C., and Coauthors, 2019: Rapid mixing and exchange of deep-ocean waters in an abyssal boundary current. *Proc. Natl. Acad. Sci. USA*, **116**, 13 233–13 238, <https://doi.org/10.1073/pnas.1904087116>.
- Pascual, A., and Coauthors, 2017: A multiplatform experiment to unravel meso- and submesoscale processes in an intense front (AlborEx). *Front. Mar. Sci.*, **4**, 39, <https://doi.org/10.3389/fmars.2017.00039>.
- Poje, A. C., and Coauthors, 2014: Submesoscale dispersion in the vicinity of the Deepwater Horizon spill. *Proc. Natl. Acad. Sci. USA*, **111**, 12 693–12 698, <https://doi.org/10.1073/pnas.1402452111>.
- Qiu, B., 1999: Seasonal eddy field modulation of the North Pacific subtropical countercurrent: TOPEX/POSEIDON observations and theory. *J. Phys. Oceanogr.*, **29**, 2471–2486, [https://doi.org/10.1175/1520-0485\(1999\)029<2471:SEFMOT>2.0.CO;2](https://doi.org/10.1175/1520-0485(1999)029<2471:SEFMOT>2.0.CO;2).
- , and S. Chen, 2004: Seasonal modulations in the eddy field of the South Pacific Ocean. *J. Phys. Oceanogr.*, **34**, 1515–1527, [https://doi.org/10.1175/1520-0485\(2004\)034<1515:SMITEF>2.0.CO;2](https://doi.org/10.1175/1520-0485(2004)034<1515:SMITEF>2.0.CO;2).
- , —, P. Klein, H. Sasaki, and Y. Sasai, 2014: Seasonal mesoscale and submesoscale eddy variability along the North Pacific subtropical countercurrent. *J. Phys. Oceanogr.*, **44**, 3079–3098, <https://doi.org/10.1175/JPO-D-14-0071.1>.
- , T. Nakano, S. Chen, and P. Klein, 2017: Submesoscale transition from geostrophic flows to internal waves in the northwestern Pacific upper ocean. *Nat. Commun.*, **8**, 14055, <https://doi.org/10.1038/ncomms14055>.
- , S. Chen, P. Klein, J. Wang, H. Torres, L.-L. Fu, and D. Menemenlis, 2018: Seasonality in transition scale from balanced to unbalanced motions in the world ocean. *J. Phys. Oceanogr.*, **48**, 591–605, <https://doi.org/10.1175/JPO-D-17-0169.1>.
- RD Instruments, 2007: WorkHorse monitor, sentinel, mariner: Acoustic Doppler current profiler: Technical manual. RD Instruments, 190 pp.
- , 2011: Acoustic Doppler current profiler principles of operation: A practical primer. RD Instruments, 52 pp.
- Rocha, C. B., S. T. Gille, T. K. Chereskin, and D. Menemenlis, 2016: Seasonality of submesoscale dynamics in the Kuroshio extension. *Geophys. Res. Lett.*, **43**, 11 304–11 311, <https://doi.org/10.1002/2016GL071349>.
- Sasaki, H., P. Klein, B. Qiu, and Y. Sasai, 2014: Impact of oceanic-scale interactions on the seasonal modulation of ocean dynamics by the atmosphere. *Nat. Commun.*, **5**, 5636, <https://doi.org/10.1038/ncomms5636>.
- Scully-Power, P., 1986: Navy oceanographer shuttle observations: STS 41-G mission report. NUSC Tech. Doc. 7611, 146 pp., <https://apps.dtic.mil/dtic/tr/fulltext/u2/a233578.pdf>.
- Shcherbina, A. Y., E. A. D’Asaro, C. M. Lee, J. M. Klymak, M. J. Molemaker, and J. C. McWilliams, 2013: Statistics of vertical vorticity, divergence, and strain in a developed submesoscale turbulence field. *Geophys. Res. Lett.*, **40**, 4706–4711, <https://doi.org/10.1002/grl.50919>.
- , and Coauthors, 2015: The LatMix summer campaign: Submesoscale stirring in the upper ocean. *Bull. Amer. Meteor. Soc.*, **96**, 1257–1279, <https://doi.org/10.1175/BAMS-D-14-00015.1>.
- Siegelman, L., 2020: Energetic submesoscale dynamics in the ocean interior. *J. Phys. Oceanogr.*, **50**, 727–749, <https://doi.org/10.1175/JPO-D-19-0253.1>.
- , P. Klein, P. Rivière, A. F. Thompson, H. S. Torres, M. Flexas, and D. Menemenlis, 2020: Enhanced upward heat transport at deep submesoscale ocean fronts. *Nat. Geosci.*, **13**, 50–55, <https://doi.org/10.1038/s41561-019-0489-1>.
- Spall, M. A., 1995: Frontogenesis, subduction, and cross-front exchange at upper ocean fronts. *J. Geophys. Res.*, **100**, 2543–2557, <https://doi.org/10.1029/94JC02860>.
- Srinivasan, K., J. C. McWilliams, L. Renault, H. G. Hristova, J. Molemaker, and W. S. Kessler, 2017: Topographic and mixed layer submesoscale currents in the near-surface southwestern tropical Pacific. *J. Phys. Oceanogr.*, **47**, 1221–1242, <https://doi.org/10.1175/JPO-D-16-0216.1>.
- , —, M. J. Molemaker, and R. Barkan, 2019: Submesoscale vortical wakes in the lee of topography. *J. Phys. Oceanogr.*, **49**, 1949–1971, <https://doi.org/10.1175/JPO-D-18-0042.1>.

- Su, Z., J. Wang, P. Klein, A. F. Thompson, and D. Menemenlis, 2018: Ocean submesoscales as a key component of the global heat budget. *Nat. Commun.*, **9**, 775, <https://doi.org/10.1038/s41467-018-02983-w>.
- , and Coauthors, 2020: High-frequency submesoscale motions enhance the upward vertical heat transport in the global ocean. *J. Geophys. Res. Oceans*, **125**, e2020JC016544, <https://doi.org/10.1029/2020JC016544>.
- Talley, L. D., 2011: *Descriptive Physical Oceanography: An Introduction*. 6th ed. Academic Press, 560 pp.
- Taylor, J. R., 2018: Accumulation and subduction of buoyant material at submesoscale fronts. *J. Phys. Oceanogr.*, **48**, 1233–1241, <https://doi.org/10.1175/JPO-D-17-0269.1>.
- Tedesco, P., J. Gula, C. Ménesguen, P. Penven, and M. Krug, 2019: Generation of submesoscale frontal eddies in the Agulhas Current. *J. Geophys. Res. Oceans*, **124**, 7606–7625, <https://doi.org/10.1029/2019JC015229>.
- Thomas, L. N., A. Tandon, and A. Mahadevan, 2008: Sub-mesoscale processes and dynamics. *Ocean Modeling in an Eddying Regime*, *Geophys. Monogr.*, Vol. 177, Amer. Geophys. Union, 17–38, <https://doi.org/10.1029/177GM04>.
- , J. R. Taylor, R. Ferrari, and T. M. Joyce, 2013: Symmetric instability in the Gulf stream. *Deep-Sea Res. II*, **91**, 96–110, <https://doi.org/10.1016/j.dsr2.2013.02.025>.
- Thompson, A. F., A. Lazar, C. Buckingham, A. C. N. Garabato, G. M. Damerell, and K. J. Heywood, 2016: Open-ocean submesoscale motions: A full seasonal cycle of mixed layer instabilities from gliders. *J. Phys. Oceanogr.*, **46**, 1285–1307, <https://doi.org/10.1175/JPO-D-15-0170.1>.
- Tomczak, M., and J. S. Godfrey, 2003: *Regional Oceanography: An Introduction*. 2nd ed. Daya Publishing House, 390 pp.
- Torres, H. S., P. Klein, D. Menemenlis, B. Qiu, Z. Su, J. Wang, S. Chen, and L. L. Fu, 2018: Partitioning ocean motions into balanced motions and internal gravity waves: A modeling study in anticipation of future space missions. *J. Geophys. Res. Oceans*, **123**, 8084–8105, <https://doi.org/10.1029/2018JC014438>.
- Vallis, G. K., 2006: *Atmospheric and Oceanic Fluid Dynamics: Fundamentals and Large-Scale Circulation*. Cambridge University Press, 745 pp.
- Xiu, P., and F. Chai, 2020: Eddies affect subsurface phytoplankton and oxygen distributions in the North Pacific Subtropical Gyre. *Geophys. Res. Lett.*, **47**, e2020GL087037, <https://doi.org/10.1029/2020GL087037>.
- Yu, X., A. C. Naveira Garabato, A. P. Martin, C. E. Buckingham, L. Brannigan, and Z. Su, 2019: An annual cycle of submesoscale vertical flow and restratification in the upper ocean. *J. Phys. Oceanogr.*, **49**, 1439–1461, <https://doi.org/10.1175/JPO-D-18-0253.1>.
- Zhang, D., T. N. Lee, W. E. Johns, C.-T. Liu, and R. Zantopp, 2001: The Kuroshio east of Taiwan: Modes of variability and relationship to interior ocean mesoscale eddies. *J. Phys. Oceanogr.*, **31**, 1054–1074, [https://doi.org/10.1175/1520-0485\(2001\)031<1054:TKEOTM>2.0.CO;2](https://doi.org/10.1175/1520-0485(2001)031<1054:TKEOTM>2.0.CO;2).
- Zhang, Z., W. Zhao, J. Tian, Q. Yang, and T. Qu, 2015a: Spatial structure and temporal variability of the zonal flow in the Luzon Strait. *J. Geophys. Res. Oceans*, **120**, 759–776, <https://doi.org/10.1002/2014JC010308>.
- , P. Li, L. Xu, C. Li, W. Zhao, J. Tian, and T. Qu, 2015b: Subthermocline eddies observed by rapid-sampling Argo floats in the subtropical northwestern Pacific Ocean in spring 2014. *Geophys. Res. Lett.*, **42**, 6438–6445, <https://doi.org/10.1002/2015GL064601>.
- , J. Tian, B. Qiu, W. Zhao, P. Chang, D. Wu, and X. Wan, 2016: Observed 3D structure, generation, and dissipation of oceanic mesoscale eddies in the South China Sea. *Sci. Rep.*, **6**, 24349, <https://doi.org/10.1038/srep24349>.
- , B. Qiu, J. Tian, W. Zhao, and X. Huang, 2018: Latitude-dependent finescale turbulent shear generations in the Pacific tropical-extratropical upper ocean. *Nat. Commun.*, **9**, 4086, <https://doi.org/10.1038/s41467-018-06260-8>.
- , Y. Zhang, B. Qiu, H. Sasaki, Z. Sun, X. Zhang, W. Zhao, and J. Tian, 2020: Spatiotemporal characteristics and generation mechanisms of submesoscale currents in the northeastern South China Sea revealed by numerical simulations. *J. Geophys. Res. Oceans*, **125**, e2019JC015404, <https://doi.org/10.1029/2019JC015404>.
- Zhong, Y., and A. Bracco, 2013: Submesoscale impacts on horizontal and vertical transport in the Gulf of Mexico. *J. Geophys. Res. Oceans*, **118**, 5651–5668, <https://doi.org/10.1002/jgrc.20402>.
- , —, J. Tian, J. Dong, W. Zhao, and Z. Zhang, 2017: Observed and simulated submesoscale vertical pump of an anticyclonic eddy in the South China Sea. *Sci. Rep.*, **7**, 44011, <https://doi.org/10.1038/srep44011>.